

# 1D atmospheric study of the temperate sub-Neptune K2-18b

D. Blain<sup>1</sup>, B. Charnay<sup>1</sup>, and B. Bézard<sup>1</sup>

LESIA, Observatoire de Paris, PSL Research University, CNRS, Sorbonne Université, Université de Paris, 92195, Meudon, France  
e-mail: doriann.blain@obspm.fr

Received July 30, 2020 / Accepted November 13, 2020

## ABSTRACT

**Context.** The atmospheric composition of exoplanets with masses between 2 and 10  $M_{\oplus}$  is poorly understood. In that regard, the sub-Neptune K2-18b, which is subject to Earth-like stellar irradiation, offers a valuable opportunity for the characterisation of such atmospheres. Previous analyses of its transmission spectrum from the Kepler, Hubble (HST), and Spitzer space telescopes data using both retrieval algorithms and forward-modelling suggest the presence of H<sub>2</sub>O and an H<sub>2</sub>-He atmosphere, but have not detected other gases, such as CH<sub>4</sub>.

**Aims.** We present simulations of the atmosphere of K2-18 b using Exo-REM, our self-consistent 1D radiative-equilibrium model, using a large grid of atmospheric parameters to infer constraints on its chemical composition.

**Methods.** We compared the transmission spectra computed by our model with the above-mentioned data (0.4 to 5  $\mu\text{m}$ ), assuming an H<sub>2</sub>-He dominated atmosphere. We investigated the effects of irradiation, eddy diffusion coefficient, internal temperature, clouds, C/O ratio, and metallicity on the atmospheric structure and transit spectrum.

**Results.** We show that our simulations favour atmospheric metallicities between 40 and 500 times solar and indicate, in some cases, the formation of H<sub>2</sub>O-ice clouds, but not liquid H<sub>2</sub>O clouds. We also confirm the findings of our previous study, which showed that CH<sub>4</sub> absorption features nominally dominate the transmission spectrum in the HST spectral range. We compare our results with results from retrieval algorithms and find that the H<sub>2</sub>O-dominated spectrum interpretation is either due to the omission of CH<sub>4</sub> absorptions or a strong overfitting of the data. Finally, we investigated different scenarios that would allow for a CH<sub>4</sub>-depleted atmosphere. We were able to fit the data to those scenarios, finding, however, that it is very unlikely for K2-18b to have a high internal temperature. A low C/O ratio ( $\approx 0.01$ – $0.1$ ) allows for H<sub>2</sub>O to dominate the transmission spectrum and can fit the data but so far, this set-up lacks a physical explanation. Simulations with a C/O ratio  $< 0.01$  are not able to fit the data satisfactorily.

**Key words.** planets and satellites: atmospheres – infrared: planetary systems – planets and satellites: gaseous planets – molecular data

## 1. Introduction

While fairly common among the thousands of exoplanets discovered to date<sup>1</sup> (see Figure 1), the atmospheres of super-Earths and sub-Neptunes – with masses between 2 and 10  $M_{\oplus}$  – are poorly understood. By essentially using the mass and radius of the planets, it has been well-established that planets with low masses ( $< 2 M_{\oplus}$ ) must primarily be made up of iron and silicates, and generally with a thin atmosphere. On the other hand, planets with high masses ( $> 10 M_{\oplus}$ ) must retain a thick atmosphere composed mainly of H<sub>2</sub> and He, representing a significant portion of the planet mass (Chen & Kipping 2016). Within the transition between the two populations, however, studies with models struggle to give a clear answer (Valencia et al. 2013; Fulton et al. 2017; Zeng et al. 2019; Otegi et al. 2020), exhibiting a degeneracy between massive rocky planets, ocean planets, and small gaseous planets. Thus, spectral observations are crucial for characterising the atmosphere of these objects and to better constrain their internal composition.

The recently discovered, transiting exoplanet K2-18b (see Table 1) offers not only the opportunity to retrieve spectroscopic data on the atmosphere of a sub-Neptune, but also to study such atmospheres under nearly Earth-like conditions. Indeed, the stellar irradiance received by K2-18b ( $E_{p,e} = 1368^{+114}_{-107} \text{ W}\cdot\text{m}^{-2}$ ) is very close to that of the Earth. Nine transits were acquired us-

ing the Wide Field Camera 3 on the Hubble Space Telescope (HST/WFC3), as well as data from Kepler K2 and Spitzer IRAC channels 1 and 2 (Benneke et al. 2019a). These data have already been analysed by several teams (Benneke et al. 2019a; Tsiraras et al. 2019; Madhusudhan et al. 2020; Scheucher et al. 2020; Bézard et al. 2020). Also, Scheucher et al. (2020) and Bézard et al. (2020) used self-consistent models (respectively, '1D-TERRA' and 'Exo-REM') to analyse the data, while the other used free retrieval algorithms. The first five investigations concluded that there is a presence of H<sub>2</sub>O as well as a significant amount of H<sub>2</sub>-He. They also derived upper limits for the abundance of CH<sub>4</sub>, which in all cases was lower than  $\approx 3.5\%$  at a 99% confidence level. In contrast, Bézard et al. (2020) found that the HST/WFC3 spectrum is dominated by CH<sub>4</sub> absorption and found abundances of CH<sub>4</sub> and H<sub>2</sub>O, respectively, between 3% and 10% and 5% and 11% at a 1- $\sigma$  confidence level. They assumed an H<sub>2</sub>-dominated atmosphere and varied the atmospheric metallicity, but their simulations did not include H<sub>2</sub>O clouds and they did not simulate non-solar C/O ratios.

Given the irradiance of the planet and the presence of H<sub>2</sub>O in the atmosphere, the question of the existence of liquid H<sub>2</sub>O is naturally posed. Benneke et al. (2019a) found that a cloud layer was needed to reproduce the data. They then used a self-consistent model and found that liquid H<sub>2</sub>O could condense at the right pressure to explain this cloud layer. Contrary to Benneke et al. (2019a), Madhusudhan et al. (2020) did not find com-

<sup>1</sup> exoplanet.eu



## 2.1. Spectroscopic data

### 2.1.1. Collision-induced absorptions

The collision-induced absorptions (CIA) included in our simulations and their references are given in Table 2. We added the contributions of the H<sub>2</sub>O–H<sub>2</sub>O CIA and, since spectroscopic data for the H<sub>2</sub>O–H<sub>2</sub> CIA were not available, of the H<sub>2</sub>O–air CIA. The reasons for this addition are detailed in Section A.

### 2.1.2. Absorption cross-sections

We calculated the absorption cross-sections of CH<sub>4</sub>, CO, CO<sub>2</sub>, FeH, H<sub>2</sub>O, H<sub>2</sub>S, HCN, K, Na, NH<sub>3</sub>, PH<sub>3</sub>, TiO, and VO at 25 pressure levels equally spaced in the log-space between 0.1 and 10<sup>7</sup> Pa. At each of these pressure levels, we calculated the cross-sections at temperatures 100, 150, 200, 250, 300, 400, 500, 600, 800, 1000, 1200, 1500, 2000, 2500, and 3000 K – except for NH<sub>3</sub>, the reasons for which are detailed below. We calculated line absorption up to a given distance ( $\Delta\nu$ ) from the line center, using the same procedure as described in Baudino et al. (2015). We used a sub-Lorentzian line profile with a  $\chi$  factor, based on Burch et al. (1969) and Hartmann et al. (2002), for, respectively, CO<sub>2</sub> and then all the other species. The cross-sections were calculated over the wavenumber range displayed in Table 3, at a resolution that is similar to the line half width.

When line lists of individual isotopes were available, we merged them by multiplying line intensities in order to reproduce the isotopic ratio found for Jupiter. Otherwise, we used the default isotopic ratio given by the database. We used H<sub>2</sub> and He pressure-broadened halfwidths ( $\gamma$ ) and temperature exponents ( $n$ ) whenever they were available. When both were available, we used a mixture of 90% H<sub>2</sub> and 10% He, which roughly corresponds to the standard Solar System He/H ratio (Lodders 2019). More details are given in Table 3 and Table 4. The specificities of some species are listed below.

CH<sub>4</sub>: We included the contribution from <sup>12</sup>CH<sub>4</sub>, <sup>13</sup>CH<sub>4</sub>, and CH<sub>3</sub>D, all taken from the TheoReTS database (Rey et al. 2017), which is more accurate than the ExoMol database. We used a <sup>12</sup>C/<sup>13</sup>C ratio of 89 (Niemann et al. 1998) and a D/H ratio of 2×10<sup>-5</sup> (Lellouch et al. 2001). We recall that the TheoReTS line list of CH<sub>3</sub>D stops at 6500 cm<sup>-1</sup>. The line list provided by the TheoReTS database separates the ‘strong lines’, which have an intensity of > 10<sup>-26</sup> cm·molecule<sup>-1</sup>, from the very-high-spectral-density ‘weak lines’, which are regrouped in ‘super lines’. This separation allows for much faster cross-section calculations, but at the price of losing information on the quantum numbers of individual lines. Hence, we had to use the same  $\gamma$  and  $n$  for all lines.

FeH, TiO and VO: H<sub>2</sub> or He  $\gamma$  and  $n$  were not available for these molecules and we used the parameters from CO.

K and Na : Given that these species have very high intensity lines (up to  $\approx 10^{-13}$  cm·molecule<sup>-1</sup>), we needed to extend our  $\Delta\nu$  up to 9000 cm<sup>-1</sup> in order to correctly account for far wing absorption. Following Burrows et al. (2000), we used a Voigt profile up to a detuning frequency of  $20 \times (T/500)^{0.6}$  cm<sup>-1</sup> for K and  $30 \times (T/500)^{0.6}$  cm<sup>-1</sup> for Na. Beyond that detuning frequency, we used the profile described by Baudino et al. (2015).

NH<sub>3</sub>: Cross-sections were calculated up to 1500 K because the line list we used lacks completeness above this temperature. We took a <sup>14</sup>N/<sup>15</sup>N ratio of 500 (Furi & Marty 2015).

PH<sub>3</sub>: The line list we used is not complete above 1000 K. However, Sousa-Silva et al. (2014) provide the PH<sub>3</sub> partition function up to 3000 K. This allows us to use the percentual loss of completeness to estimate the proportion of missing opacity, as suggested in the cited work.

### 2.1.3. $k$ -coefficients

We used these high-resolution absorption coefficients to calculate  $k$ -coefficients according to the method described in Baudino et al. (2015), using 16 Gauss-Legendre quadrature points (eight for values of the cumulative distribution of the absorption coefficients between 0 and 0.95, and eight between 0.95 and 1). Four sets of  $k$ -coefficients were calculated, at resolutions of 0.5, 20, 200, and 2000 cm<sup>-1</sup>, although only the 20 cm<sup>-1</sup> step one was used in the main part of this study.

## 2.2. Radiative-convective equilibrium model: stellar irradiance

We added the planetary averaged stellar irradiance  $E_{\downarrow, e, \nu}$  reaching the planet to Exo-REM. We used stellar spectra from the BT-Settl model (Allard et al. 2012). We chose a spectrum modelled at an effective temperature  $T_S = 3500$  K,  $\log_{10}(g[\text{cm} \cdot \text{s}^{-2}]) = 5$ , a null metallicity and no alpha enhancement. We neglected the spectral dependency on surface gravity and metallicity. Then we interpolated the BT-Settl spectrum on a spectral grid with a 0.1 cm<sup>-1</sup> wavenumber step. This interpolated spectrum was then convolved at the resolution of Exo-REM flux calculations (see Section 3) to obtain the modelled radiosity  $J_{S, e, \nu}$ . Then we obtained  $E_{\downarrow, e, \nu}$  from:

$$E_{\downarrow, e, \nu} = \frac{1}{4} J_{S, e, \nu} \frac{J_{B, e, \nu}(T_{*, \text{eff}})}{J_{B, e, \nu}(T_{S, \text{eff}})} \left( \frac{R_*}{a_p} \right)^2, \quad (1)$$

where  $J_{B, e, \nu}(T)$  is the radiosity of a black body at temperature,  $T$ , and  $T_{*, \text{eff}}$  is the effective temperature of the star,  $R_*$  is the radius of the star,  $a_p$  is the distance between the star and the planet, and the geometric factor 1/4 is used to represent planet-averaged conditions. The ratio of the  $J_{B, e, \nu}$  terms is used to obtain a stellar spectrum at the effective temperature of K2-18. This was done instead of interpolating on the BT-Settl grid as  $T_{S, \text{eff}}$  is close to  $T_{*, \text{eff}}$ .

## 2.3. Atmospheric model: thermochemistry

We used the recommended present atomic solar system abundances given by Lodders (2019) to define our standard abundances and our reference metallicity  $((Z/H)_{\odot})$ . The atomic abundances at a metallicity  $Z/H$  are obtained by keeping the H, He, Ne, Ar, Kr, and Xe standard abundances constant while multiplying the standard abundances of other elements by  $Z/H$ . The list of all the species included in our thermochemical calculations is displayed in Table 5. It is possible to adjust the abundances of all individual elements listed in this table, although it is always assumed that the atmosphere is dominated by H<sub>2</sub>, limiting Exo-REM capabilities to metallicities  $\lesssim 1000 (Z/H)_{\odot}$ . We included species that either: significantly affect the volume mixing ratio

Table 2: Collision-induced absorption references

CIA	References
H <sub>2</sub> – H <sub>2</sub>	1, 2, 3
H <sub>2</sub> – He	3
H <sub>2</sub> O – H <sub>2</sub> O	4

**References.** (1) Borysow et al. (2001); (2) Borysow (2002); (3) Richard et al. (2012); (4) Mlawer et al. (2012).

Table 3: Species cross-section parameters

Species	Wavenumber range (cm <sup>-1</sup> )	$\Delta\nu$ (cm <sup>-1</sup> )	Intensity cutoff (cm <sup>-1</sup> molecule <sup>-1</sup> )	Line list
CH <sub>4</sub>	30 – 13330	250	10 <sup>-36</sup> at 2000 K	TheoReTS (1)
CO	30 – 8330	120	10 <sup>-27</sup> at 3000 K	HITEMP (2)
CO <sub>2</sub>	30 – 8130	120	10 <sup>-25</sup> at 3000 K	HITEMP (2)
FeH	30 – 14830	120	10 <sup>-30</sup> at 4000 K	ExoMol (3)
H <sub>2</sub> O	30 – 26430	120	10 <sup>-27</sup> at 2000 K	HITEMP (2)
H <sub>2</sub> S	30 – 10830	120	10 <sup>-27</sup> at 2000 K	ExoMol (4)
HCN	30 – 12530	120	10 <sup>-25</sup> at 3000 K	ExoMol (5)
K	1030 – 50030	9000	10 <sup>-27</sup> at 2500 K	NIST (6)
Na	1030 – 50030	9000	10 <sup>-27</sup> at 2500 K	NIST (6)
NH <sub>3</sub>	30 – 11830	120	10 <sup>-30</sup> at 1500 K	ExoMol (7, 8)
PH <sub>3</sub>	30 – 9830	120	10 <sup>-30</sup> at 2500 K	ExoMol (9)
TiO	230 – 29230	120	10 <sup>-30</sup> at 4000 K	ExoMol (10)
VO	30 – 19830	120	10 <sup>-30</sup> at 4000 K	ExoMol (11)

**References.** (1) Rey et al. (2017); (2) Rothman et al. (2010); (3) Bernath (2020); (4) Azzam et al. (2016); (5) Harris et al. (2006); (6) Kramida et al. (2019); (7) Coles et al. (2019); (8) Yurchenko (2015); (9) Sousa-Silva et al. (2014); (10) Schwenke (1998); (11) McKemmish et al. (2016).

Table 4: Line broadening references

Species	$\gamma$ references	$n$ references
CH <sub>4</sub>	H <sub>2</sub> – He (1, 2)	Idem
CH <sub>3</sub> D	H <sub>2</sub> (3)	Idem
CO	H <sub>2</sub> – He (4)	Idem
CO <sub>2</sub>	H <sub>2</sub> – He (5)	Air (6)
FeH	Same as CO	Idem
H <sub>2</sub> O	H <sub>2</sub> (7)	Air (6)
H <sub>2</sub> S	H <sub>2</sub> (8)	Air (6)
HCN	N <sub>2</sub> (9)	Idem
K	H <sub>2</sub> (10)	Idem
Na	H <sub>2</sub> (11)	Idem
NH <sub>3</sub>	H <sub>2</sub> – He (12, 13)	Idem
PH <sub>3</sub>	H <sub>2</sub> – He (14)	Idem
TiO	Same as CO	Idem
VO	Same as CO	Idem

**References.** (1) Pine (1992); (2) Margolis (1996); (3) Lerot et al. (2003); (4) Wilzewski et al. (2016); (5) Burch et al. (1969); (6) Rothman et al. (2010); (7) Langlois et al. (1994); (8) Kissel et al. (2002); (9) Rinsland et al. (2003); (10) Allard et al. (2016); (11) Allard et al. (2012); (12) Nemtchinov et al. (2004); (13) Brown & Peterson (1994); (14) see Baudino et al. (2015).

(VMR) profiles of our absorbing species (see Section 2.1.2), are susceptible to the formation of a major cloud layer, or substantially impact the molar mass of the atmosphere (according to Lodders 2010).

Most of the equilibrium abundances are derived from the equation of conservation of each species, using the standard Gibbs free energy of formation  $\Delta G_f^\circ$  listed in Chase (1998). For PH<sub>3</sub>(g), we used the  $\Delta G_f^\circ$  from Lodders (1999), while for MnS(cr,l) and ZnS(cr,l), we used the values from Robie & Hemingway (1995), and for CaTiO<sub>3</sub>(cr) we used values from Wood-

field et al. (1999). We used a grid of temperatures between 200 and 4000 K, with a 100 K step, to map our  $\Delta G_f^\circ$ . When the temperature range of the references used were smaller than our target temperature range, we used a linear extrapolation to fill up our grid. The  $\Delta G_f^\circ$  at a given temperature are linearly interpolated from this grid. We calculated the saturation pressure of the following species directly: H<sub>2</sub>O (Wagner & Pruss 1993; Wagner et al. 1994; Lin et al. 2004; Fray & Schmitt 2009), NH<sub>3</sub> (Fray & Schmitt 2009; Lide 2009), and NH<sub>4</sub>SH (Stull 1947). We used a very simplified Ca-Al-Ti chemistry compared to, for instance,

Lodders (2002), but the impact on our simulations was expected to be limited. We simulated the formation of Fe–Ni alloys by treating the Fe independently while keeping the Ni(g)/Fe(g) ratio constant. We considered the formation of  $\text{H}_3\text{PO}_4$  instead of  $\text{P}_4\text{O}_6$ , based on the results of Wang et al. (2016).

We included non-equilibrium processes in the  $\text{CH}_4$ –CO, CO–CO<sub>2</sub>, N<sub>2</sub>–NH<sub>3</sub>–HCN chemical systems following the approach of Zahnle & Marley (2014). The chemical quenching level is determined by equating a reaction timescale to the mixing time  $H^2/K_{zz}$ , where  $H$  is the atmospheric scale height and  $K_{zz}$  the eddy mixing coefficient. Below the quenching level, the abundance profiles of the relevant species are governed by thermochemical equilibrium while, above this level, the mixing ratios of the quenched species are held constant. We used the chemical reaction timescales given by Eqs. 12–14 for  $\text{CH}_4$ –CO, Eq. 44 for CO–CO<sub>2</sub>, Eq. 32 for NH<sub>3</sub>–N<sub>2</sub>, and Eq. 40 for HCN–NH<sub>3</sub>–N<sub>2</sub> in Zahnle & Marley (2014). In the case of PH<sub>3</sub>, we assume that its conversion to  $\text{H}_3\text{PO}_4$  is inhibited, as observed in the giant planets of our solar system. We compared our chemical model in the case of K2-18b (taking identical temperature profile, elemental abundances, and eddy diffusion coefficient) against the model described in Venot et al. (2020)<sup>4</sup>. For CO, HCN, and NH<sub>3</sub>, we found VMR differences lower than 20% with our model in the HST sensitivity region, and lower than 2% in the case of CH<sub>4</sub> and H<sub>2</sub>O. The difference is larger for CO<sub>2</sub>, with our VMR being 25% higher than the value found in O. Venot’s model. We consider these differences to be satisfactory.

### 3. Methodology

The star and planetary parameters used in our simulations are displayed in Table 1. A summary of our model grid is displayed in Table 6. We took a planetary radius at 10<sup>5</sup> Pa of  $R_p = 16400$  km, which is slightly different from the value used by Benneke et al. (2019a) (who define  $R_p$  as the radius at 10<sup>3</sup> Pa), because it is closer to the radius we find when fitting the observed data. To compare our model spectrum with the data, we applied an offset on  $R_p$  in the calculation of the transit depth, such that the  $\chi^2$  is minimised.

The internal temperature resulting from the residual heat of formation of the planet was calculated following (Rogers & Seager 2010):

$$T_{p,\text{int}} = \left( \frac{L_{\text{int}}}{4\pi\sigma R_p^2} \right)^{1/4}, \quad (2)$$

where  $L_{\text{int}}$  is obtained from (Rogers & Seager 2010):

$$\begin{aligned} \log_{10} \left( \frac{L_{\text{int}}}{L_{\odot}} \right) = & a_1 + a_{M_p} \log_{10} \left( \frac{M_p}{M_{\oplus}} \right) \\ & + a_{R_p} \log_{10} \left( \frac{R_p}{R_{\oplus}} \right) \\ & + a_{t_p} \log_{10} \left( \frac{t_p}{1 \text{ Gyr}} \right), \end{aligned} \quad (3)$$

where  $a_1 = -12.46 \pm 0.05$ ,  $a_{M_p} = 1.74 \pm 0.03$ ,  $a_{R_p} = -0.94 \pm 0.09$ ,  $a_{t_p} = -1.04 \pm 0.04$ ,  $t_p$  is the age of the planet, and the astronomical constants are defined by the International Astronomical Union (IAU, Mamajek et al. 2015). According to a gyrochronological model from Guinan & Engle (2019), the age of K2-18

can be estimated at  $2.4 \pm 0.6$  Gyr. Assuming that K2-18b ended its formation a few Myr after the formation of its star (so that  $t_* \approx t_p$ ), like what happened in our solar system, we obtained from Equation 2  $T_{p,\text{int}} \approx 83^{+8}_{-6}$  K. Rounding down this value, we chose 80 K as our nominal internal temperature.

The net fluxes are calculated from 40 to 30000 cm<sup>-1</sup>, with a step of 20 cm<sup>-1</sup>. The atmospheric grid consists of 81 levels equally spaced in the log-space between 0.1 and 10<sup>7</sup> Pa. We imposed a correlation length of 0.5 pressure scale height to the solution temperature profile in order to avoid non physical oscillations (see Baudino et al. 2015). We considered cloud radiative effects and scattering only from H<sub>2</sub>O clouds. The NH<sub>3</sub> and NH<sub>4</sub>SH clouds would form in atmospheres that are colder than what is expected for K2-18b, while NH<sub>4</sub>Cl clouds are too thin to have a significant impact, and other clouds are condensing too deeply into the atmosphere (see Section 4.2). Cloud vertical mass mixing ratios are calculated assuming equilibrium between the downward flux of falling particles and the upward flux of gas and cloud particles due to advection and turbulent mixing (see Charnay et al. 2018).

When we change the irradiance of the planet by a factor of  $k$ , we do so by multiplying  $a_p$  by  $1/\sqrt{k}$  (see Equation 1). We proceed this way to make model comparison easier. Indeed,  $a_p$  impacts only the irradiance, while the two other parameters,  $T_{*,\text{eff}}$  and  $R_*$ , affects respectively the stellar spectrum and both the stellar spectrum and the transmission spectrum.

We estimated  $K_{zz}$  using the values derived by Exo-REM (see Charnay et al. 2018). We found that typical  $K_{zz}$  values for K2-18b range from 10<sup>6</sup> to 10<sup>9</sup> cm<sup>2</sup>·s<sup>-1</sup>, with the highest values found in the convective layers. Given the uncertainties on the estimation of  $K_{zz}$ , we enlarged this range to 10<sup>5</sup>–10<sup>10</sup> cm<sup>2</sup>·s<sup>-1</sup>. We also found that a quenching of our species often occurs just below the uppermost convective layer (see Section 4.3), hence, we set our nominal  $K_{zz}$  value at 10<sup>6</sup> cm<sup>2</sup>·s<sup>-1</sup>.

We used a fractional area covered by clouds  $f_c = 0.15$  for the calculation of the temperature profile, and  $f_c = 1.0$  for the calculation of the transmission spectra. To ensure numerical stability, the cloud mean particle radius,  $r$ , was fixed at a constant value (50 μm) that roughly corresponds to the maximum one predicted by the Exo-REM self-consistent cloud model at 300 (Z/H)<sub>⊙</sub> and nominal irradiation (see Charnay et al. 2018, and Section 4.2), unless stated otherwise. We call this our nominal model. We explore the effects of changing some of these parameters in the following sections.

## 4. Results

### 4.1. Metallicity and irradiance

Here, we assume that K2-18b has retained a relatively thick H<sub>2</sub>–He atmosphere. This atmosphere can be enriched in heavy elements – compared to the initial proto-stellar nebula – during the formation of the planet via collisions with planetesimals (Fortney et al. 2013). There could also be a contribution from the erosion of the primordial core (Iaroslavit & Podolak 2007).

In Figure 2, we show our best fit for the dataset of Benneke et al. (2019a) at nominal irradiation, along with the HST data reduced by Tsiaras et al. (2019). The contributions of the different opacity sources to this spectrum are represented in Figure 3. The temperature profile and VMR of this spectrum are represented respectively in Figure 4 and Figure 5. Because the stellar spectrum we used is slightly more intense than a black body between  $\approx 1$  and 2.5 μm, the temperatures we obtain in the upper atmosphere are slightly higher ( $\approx 5$  K at 1 kPa) than what would be

<sup>4</sup> O. Venot, private communication. The comparison was made using the "nominal model" described in Section 4.1

Table 5: Species included in thermochemical calculations.

Element	Standard abundance ( $\times 10^{-6}$ )	Gases	Condensates
H	10 <sup>6</sup>	H <sub>2</sub> <sup>*</sup> , H, H <sub>2</sub> O <sup>*</sup> , CH <sub>4</sub> <sup>*</sup> , ...	
He	83950	He <sup>*</sup>	
C <sup>a</sup>	295	CH <sub>4</sub> <sup>*</sup> , CO <sup>*</sup> , CO <sub>2</sub> <sup>*</sup> , HCN <sup>*</sup>	
N <sup>a</sup>	70.8	NH <sub>3</sub> <sup>*</sup> , N <sub>2</sub> , HCN <sup>*</sup>	NH <sub>3</sub> , NH <sub>4</sub> SH, NH <sub>4</sub> Cl
O <sup>a</sup>	537	H <sub>2</sub> O <sup>*</sup> , CO <sup>*</sup> , CO <sub>2</sub> <sup>*</sup> , SiO	H <sub>2</sub> O, Mg <sub>2</sub> SiO <sub>4</sub> , MgSiO <sub>3</sub> , SiO <sub>2</sub> , Al <sub>2</sub> O <sub>3</sub> , Cr <sub>2</sub> O <sub>3</sub>
Ne	141	Ne	
Na	1.26	Na <sup>*</sup> , NaCl	Na <sub>2</sub> S
Mg	33.1	Mg	Mg <sub>2</sub> SiO <sub>4</sub> , MgSiO <sub>3</sub>
Al	2.63	Al	Al <sub>2</sub> O <sub>3</sub>
Si	32.4	SiO, SiH <sub>4</sub>	Mg <sub>2</sub> SiO <sub>4</sub> , MgSiO <sub>3</sub> , SiO <sub>2</sub>
P	0.269	PH <sub>3</sub> <sup>*</sup> , PH <sub>2</sub> , PO, P <sub>2</sub>	H <sub>3</sub> PO <sub>4</sub> <sup>b</sup>
S	14.1	H <sub>2</sub> S <sup>*</sup>	NH <sub>4</sub> SH, Na <sub>2</sub> S, MnS, ZnS
Cl	0.17	HCl, NaCl, KCl	NH <sub>4</sub> Cl, KCl
Ar	3.16	Ar	
K	0.117	K <sup>*</sup> , KCl	KCl
Ca	1.86	Ca	CaTiO <sub>3</sub>
Ti	0.0794	Ti, TiO <sup>*</sup> , TiO <sub>2</sub>	TiN, CaTiO <sub>3</sub>
V	0.00891	V, VO <sup>*</sup> , VO <sub>2</sub>	VO, CaTiO <sub>3</sub> <sup>c</sup>
Cr	0.427	Cr	Cr, Cr <sub>2</sub> O <sub>3</sub>
Mn	0.295	Mn	MnS
Fe	28.2	Fe, FeH <sup>*</sup>	Fe
Ni	1.58	Ni	Fe <sup>d</sup>
Zn	0.0407	Zn	ZnS
Kr	0.00166	Kr	
Xe	0.00018	Xe	

**Notes.** Elements are classed by increasing atomic number. Elements not displayed are not taken into account. Aside from H, are mentioned only the species affecting the element equilibrium (i.e. TiO, VO and PO do not affect the abundance of O). <sup>(a)</sup> Non-equilibrium chemistry based on a comparison of chemical time constants with vertical mixing time from Zahnle & Marley (2014). <sup>(b)</sup> Only at equilibrium. <sup>(c)</sup> Dissolution of VO into CaTiO<sub>3</sub>, assuming an ideal solid solution and Henri's law. <sup>(d)</sup> Formation of Fe-Ni alloys. <sup>(e)</sup> Species for which lines and/or CIA are taken into account.

Table 6: Model grid

Parameter	Range	Nominal value
Metallicity ( $(Z/H)_{\odot}$ )	1–1000	175
C/H ( $(C/H)_{\odot}$ )	0.3–1000	175
Irradiance ( $E_{p,e}$ )	0.5–1.5	1
$K_{zz}$ ( $\text{cm}^2 \cdot \text{s}^{-1}$ )	$10^5$ – $10^{10}$	$10^6$
$r$ ( $\mu\text{m}$ )	20–600	50
$T_{p,int}$ (K)	45–200	80

obtained with a black body at the effective temperature of the star. The prevalence of CH<sub>4</sub> absorptions over H<sub>2</sub>O absorptions is discussed in Section 5.1.

In Figure 6, we display the  $\chi^2$  of our nominal models for the datasets from Benneke et al. (2019a) and Tsiaras et al. (2019), including their respective reduction of the same HST raw data, as well as in both cases the K2 and Spitzer data from Benneke et al. (2019a). We performed simulations of K2-18b for 1, 3, 10, 30, 50, 75, 100, 125, 150, 175, 200, 300, 400, 500, and 1000 times  $(Z/H)_{\odot}$  and for irradiances between 0.5 and 1.5 time the nominal irradiation, with a step of 0.1. We consider a model as statistically accurate if it can reproduce the data within the  $1\sigma$  confidence level (68%). Since there are 20 data points, we have 20 to 1 degrees of freedom, so the  $1\sigma$  confidence level corresponds to a  $\chi^2$  of 21.36. While the dataset from Tsiaras et al. (2019) allows, according to our interpolation, for metallicities

$\geq 65 (Z/H)_{\odot}$  within K2-18b irradiation  $3\sigma$  uncertainties, the dataset from Benneke et al. (2019a) is much more restrictive, allowing only a metallicity between 100 and 200  $(Z/H)_{\odot}$  at 0.9 times the nominal irradiation, or a metallicity between 150 and 200  $(Z/H)_{\odot}$  at or above the nominal irradiation. These values are within the most common range of metallicity predicted by Fortney et al. (2013) for planets with radius in the 2–4  $R_{\oplus}$  range (between 100 and 400+  $(Z/H)_{\odot}$ ). At nominal irradiation, our best fit against Benneke et al. (2019a) and Tsiaras et al. (2019) data is located respectively at 175  $(Z/H)_{\odot}$  ( $\chi^2 = 21.07$ ) and 150  $(Z/H)_{\odot}$  ( $\chi^2 = 17.24$ ). In both cases, there is no H<sub>2</sub>O cloud formation, and we derive a Bond albedo of respectively 0.017 and 0.018.

The relationship between temperature, metallicity, and goodness of fit presented in Figure 6 can be explained as follows. The amplitudes of the features in the transmission spectra are correlated with the abundance of absorbers in the atmosphere as well

as to its scale height, which can be written as

$$H = \frac{RT}{\mu g}, \quad (4)$$

where  $R$  is the gas constant, and  $T$ ,  $\mu$  and,  $g$  are respectively the temperature, the molar mass and the gravity in an atmospheric layer. As the metallicity decreases, two concurrent effects are occurring. The diminution of the VMR of absorbers in the atmosphere will of course decrease the spectrum amplitude. However, decreasing the VMR of heavy species will also leads to a decrease of  $\mu$ , and thus to an increase of the amplitudes. This latter effect is dominant in our simulations for metallicities  $\geq 10 (Z/H)_\odot$ , as illustrated in Figure 7. At lower metallicities, heavy elements contribute to less than 10% of  $\mu$ , so the effect of less intense gas absorptions becomes dominant, flattening the transmission spectrum. If we decrease irradiation, the atmosphere gets colder and H<sub>2</sub>O clouds start to form and to thicken, flattening the spectrum at transparent wavelengths where part of the transmitted stellar light reaches the condensation level. As stellar irradiation decreases, the cloud forms lower and lower in the atmosphere, eventually ending below the region probed by transit spectroscopy where it can no longer directly affect the spectrum. The condensation also removes more gaseous H<sub>2</sub>O, decreasing  $\mu$  and H<sub>2</sub>O absorption. On the other hand, increasing the irradiation leads to an increase of the temperatures, and, hence, of the scale height and of the absorption amplitudes, as shown in Figure 8.

#### 4.2. Clouds

In Figure 9, we show that H<sub>2</sub>O cloud can form at nominal irradiation and metallicities above 200  $(Z/H)_\odot$ . At 300  $(Z/H)_\odot$ , the cloud forms at 1 kPa. However, this cloud cannot form even at 1000  $(Z/H)_\odot$  if the irradiation is more than 10% higher than the nominal irradiation. As a general tendency, the H<sub>2</sub>O cloud forms lower in the atmosphere as the irradiation decreases and the metallicity increases. This is because as the irradiation decreases, the temperature decreases, so the temperature profile crosses the H<sub>2</sub>O condensation profile at higher pressures. Also, as the metallicity increases, the partial pressure of H<sub>2</sub>O increases, shifting its condensation profile towards higher temperatures.

The effect of H<sub>2</sub>O clouds at nominal irradiation on the temperature profile is insignificant, but its effect on the transmission spectrum is quite important, as shown in Figure 10. The cloud shields the transit spectrum from the star light passing below its altitude, with a particularly strong effect in the visible range. The cloud also has a slight effect on the Bond albedo, as shown in Figure 11. Under 200  $(Z/H)_\odot$ , increasing the metallicity decreases the Bond albedo, because there is more and more gas absorption. At 300  $(Z/H)_\odot$ , adding clouds increases the Bond albedo from 0.017 to 0.018. This effect then increases with metallicity, because the cloud thickens and, thus, it is able to reflect more light. We note that above 300  $(Z/H)_\odot$ , the Bond albedo increases with metallicity even without clouds. This is due to the removal of gaseous H<sub>2</sub>O from the atmosphere.

We were unable to make Exo-REM simulations converge at nominal irradiation when using its self-consistent cloud mode (Charnay et al. 2018). In this mode, the mean particle radius is determined from a comparison of the timescales of the micro-physical processes governing the formation and growth of cloud particles. This is likely due to the temperature profile barely crossing the H<sub>2</sub>O saturation profile, so that a slight variation of

temperature in the solution profile can have a major effect on cloud formation. Nevertheless, we were able to determine that the H<sub>2</sub>O cloud particles, according to Exo-REM, should be between 20 and 50  $\mu\text{m}$  at 300  $(Z/H)_\odot$ , for a calculated  $K_{zz}$  of  $\approx 9 \times 10^7 \text{ cm}^2 \cdot \text{s}^{-1}$  at the layer of condensation. The result is essentially the same if we fix the sedimentation parameter ( $f_{\text{sed}}$ ) between 1 and 5, which is typical of the clouds in the solar system (see Charnay et al. 2018). If we fix  $K_{zz}$  at  $10^{10} \text{ cm}^2 \cdot \text{s}^{-1}$  and  $f_{\text{sed}}$  at 5, we obtain a maximum mean cloud particle radius of 600  $\mu\text{m}$ . In Figure 12, we show the effect of the mean cloud particle radius on the transmission spectrum. As the mean radius increases, the effect of the cloud is less and less visible. At 600  $\mu\text{m}$ , it is almost indistinguishable from the spectrum without clouds.

We found that in our simulations, liquid H<sub>2</sub>O clouds can form at irradiations lower than 80% of the nominal irradiation, which is slightly lower than the  $3\sigma$  lower uncertainty of K2-18b irradiation. However, according to Figure 6, this case is not favoured by the data, and is above the  $1\sigma$  confidence level against Benneke et al. (2019a) data. It is not surprising that our results for the likelihood of liquid H<sub>2</sub>O differ from Benneke et al. (2019a), even though they also used a self-consistent model in their demonstration. Indeed, they assumed an albedo of 0.3, which is much higher than what we found. They probably also included a much lower amount of CH<sub>4</sub>, which significantly reduces the stellar heating.

We note from Figure 4 that aside from H<sub>2</sub>O, clouds of NH<sub>4</sub>Cl, KCl, ZnS and Na<sub>2</sub>S are condensing within our pressure grid. Clouds below KCl (included) form too low in the atmosphere to significantly impact the temperature profile above the convective layers, so they can safely be ignored. This is not the case for NH<sub>4</sub>Cl. According to our simulations, NH<sub>4</sub>Cl removes  $\approx 30\%$  of the total amount of Cl in the atmosphere, with the remaining 70% being removed mainly via the condensation of KCl, RbCl, and CsCl. The latter two are not included in Exo-REM, the condensation of RbCl and CsCl removing less than 0.15% of the Cl, assuming a standard composition. While the NH<sub>4</sub>Cl cloud is, to our knowledge, rarely mentioned in the exoplanet literature, it offers an explanation to the lack of Cl-bearing species in the upper atmosphere of the giant planets of our solar system (Fouchet et al. 2004; Teanby et al. 2006). Nevertheless, we found that with our nominal model, NH<sub>4</sub>Cl clouds with  $r = 5 \mu\text{m}$  – roughly the minimum value found by the Exo-REM self-consistent cloud model on the layer with the most particles – have essentially no impact on the temperature profile and a marginal impact on the visual part of the transmission spectrum<sup>5</sup>, lowering the  $\chi^2$  against Benneke et al. (2019a) data by  $\approx 0.2$ . Therefore, they can probably be neglected for K2-18b, but they might play a more important role in the transmission spectra of slightly hotter planets.

#### 4.3. Eddy diffusion coefficient and internal temperature

In Figure 13, we represented the temperature profiles and VMRs obtained with our upper and lower uncertainty boundaries on the internal temperature of K2-18b (assuming  $t_p$  between 1 and 13 Gyr), as well as our selected nominal value (80 K). It appears that the internal temperature has only a minor effect on the temperature profile, except in the deepest layers of the atmosphere. This effect was also noted by other authors such as Morley et al.

<sup>5</sup> NH<sub>4</sub>Cl optical constants were not available, and we used the parameters from NH<sub>4</sub>SH. Both molecules show similar strong absorptions due to NH<sub>4</sub><sup>+</sup> and minor contributions from Cl<sup>-</sup> or HS<sup>-</sup> (NIST chemical Web-Book and Howett et al. 2007).

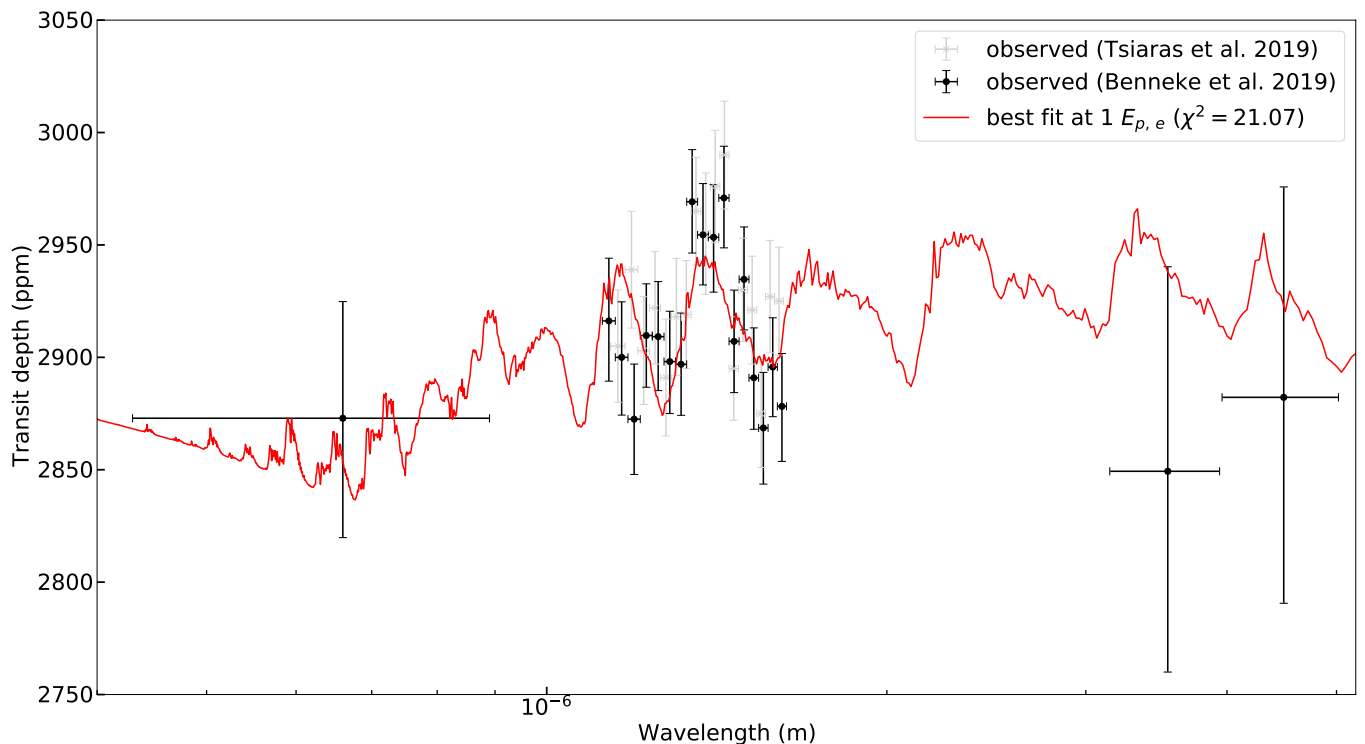


Fig. 2: Best fit of our model to the dataset of Benneke et al. (2019a) at nominal irradiation ( $1368 \text{ W}\cdot\text{m}^{-2}$ ). Black: K2, HST and Spitzer data from Benneke et al. (2019a). Grey: HST data from Tsiaras et al. (2019). Red: Exo-REM transmission spectrum at 175  $(Z/H)_{\odot}$ , with an offset of the  $10^5$ -Pa level of  $-5 \text{ km}$ . The  $\chi^2$  of this spectrum against Benneke et al. (2019a) data is indicated in parentheses.

Table 7: Best fits against Benneke et al. (2019a) dataset as a function of internal temperature.

$T_{p,\text{int}}$ (K)	$(Z/H)_{\odot}$	$K_{zz}$ ( $\text{cm}^2\cdot\text{s}^{-1}$ )	$\chi^2$
45	175	$10^8$	20.61
80	175	$10^{10}$	21.00
115	175	$10^{10}$	21.00

(2017). This is because the received flux (the stellar irradiance) is two to three orders of magnitude higher than the internal flux. Hence, above the convective layers (here at  $\approx 20 \text{ kPa}$ ), the difference of temperature between our two extreme simulations is less than 40 K (8 K on average). However, below the convective layers ( $\approx 200 \text{ kPa}$ ), the atmosphere is opaque, thus, the stellar irradiance can no longer heat the atmosphere and the internal heating become prominent. Consequently, at the bottom of our pressure grid, the difference in temperature between our two extreme models reaches  $\approx 500 \text{ K}$ . This affects the species abundances, in the upper atmosphere as well if the quench level of a species is at a pressure level below the region of stellar heating.

In Figure 14, we show the effect of the eddy diffusion coefficient on the VMR of the main C-, N-, and O-bearing species at 175  $(Z/H)_{\odot}$ . The VMR at thermochemical equilibrium are also displayed. The main effect of increasing  $K_{zz}$  is to shift down the quench levels of the species.

In Figure 15, we display the VMR of  $\text{CH}_4$ ,  $\text{CO}$ , and  $\text{H}_2\text{O}$  for  $K_{zz} = 10^6$ ,  $10^8$ , and  $10^{10} \text{ cm}^2\cdot\text{s}^{-1}$  as a function of the age of the planet and the corresponding internal temperature (see Equation 2). As the internal temperature decreases (or as the planet

gets older), the impact of the  $K_{zz}$  on these VMR gets smaller. If the  $K_{zz}$  is low ( $\lesssim 10^6 \text{ cm}^2\cdot\text{s}^{-1}$ ), the chemical composition of the atmosphere essentially does not change. On the other hand, under vigorous mixing, the chemical composition of the upper atmosphere can be significantly altered over time. With  $K_{zz} \gtrsim 10^{10} \text{ cm}^2\cdot\text{s}^{-1}$ , if the planet is young ( $\lesssim 1 \text{ Gyr}$  or  $T_{p,\text{int}} \gtrsim 100 \text{ K}$ ),  $\text{CO}$  could become the dominant O-bearing species and remain more abundant than  $\text{CH}_4$  for several Gyr. In parallel,  $K_{zz}$  could also decrease over time, as the heat to be dissipated by convection decreases. Moreover, if the quench level switches from a convective layer to a radiative one,  $K_{zz}$  could drop by several orders of magnitude, rapidly changing the chemistry of the upper atmosphere if this occurs when the planet is still young.

We compared our simulations within our range of  $K_{zz}$ , at  $T_{p,\text{int}}$  of 45, 80, and 115 K and at metallicities of 50, 75, 100, 125, 150, 175, 200, and 300  $(Z/H)_{\odot}$ . The best-fit parameters against Benneke et al. (2019a) data for each tested internal temperature can be found in Table 7. We found no significant differences at constant metallicity in terms of goodness of fit for the tested  $T_{p,\text{int}}$ , the  $\chi^2$  value varying by less than 0.7 across all  $K_{zz}$  values. In each case, our best fit is located at 175  $(Z/H)_{\odot}$ . The slight difference in goodness of fit at  $T_{p,\text{int}} = 45 \text{ K}$  compared to the other tested internal temperatures is due to  $\text{H}_2\text{O}$  cloud condensation occurring in the former case and not in the latter.  $\chi^2$  values above 200 and below 150  $(Z/H)_{\odot}$  are systematically above the  $1\sigma$  confidence level. We note that even at 175  $(Z/H)_{\odot}$ ,  $T_{p,\text{int}} = 115 \text{ K}$  and  $K_{zz} = 10^{10} \text{ cm}^2\cdot\text{s}^{-1}$ , we retrieve a  $\text{CH}_4$  VMR above 1.5% in the upper atmosphere. Hence, internal heating from a relatively young ( $t_p \approx 1 \text{ Gyr}$ ) K2-18b and

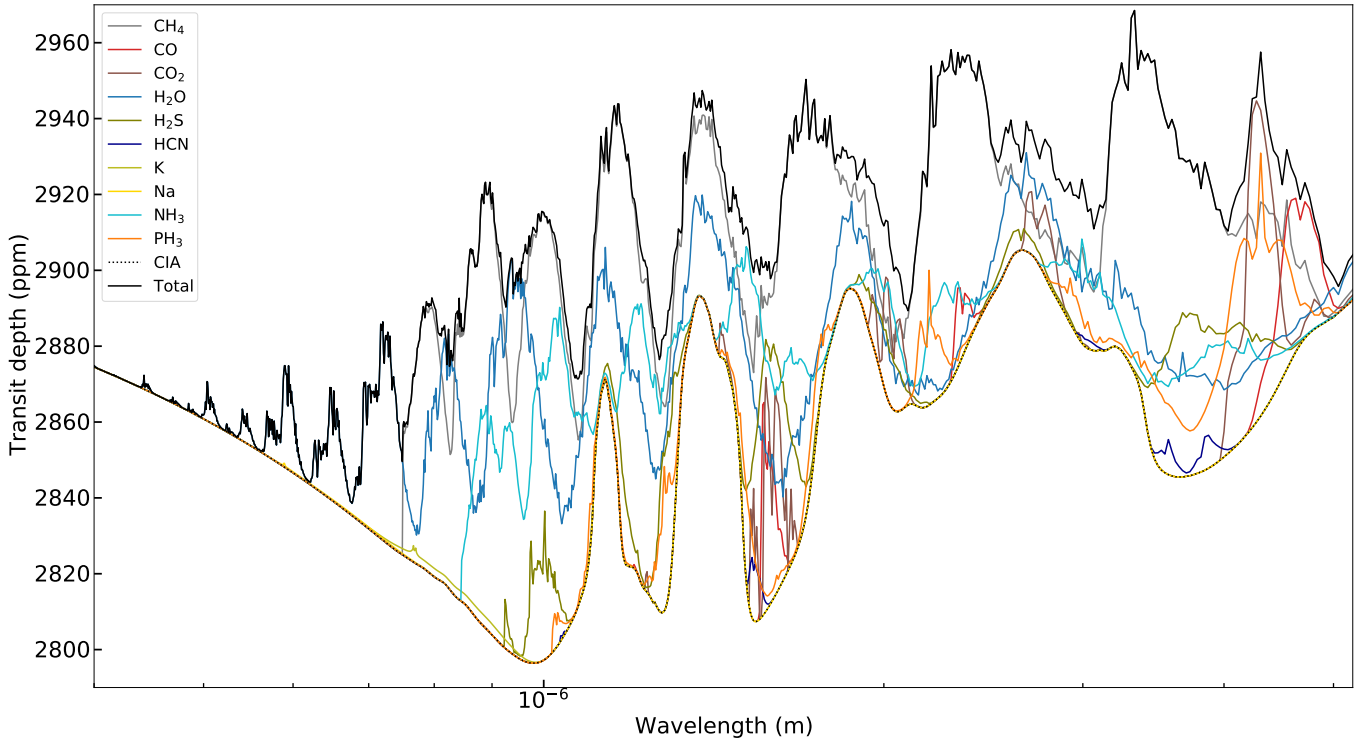


Fig. 3: Contributions of the absorbing species to our best-fit transmission spectrum at nominal irradiation within the K2 to Spitzer spectral range. The H<sub>2</sub>O cloud is not forming in this case, so there is no cloud contribution. The spectral contribution of individual species takes the CIA and Rayleigh scattering (represented as a dotted curve) into account. The spectral contribution of FeH, TiO, and VO are not represented here as they are insignificant.

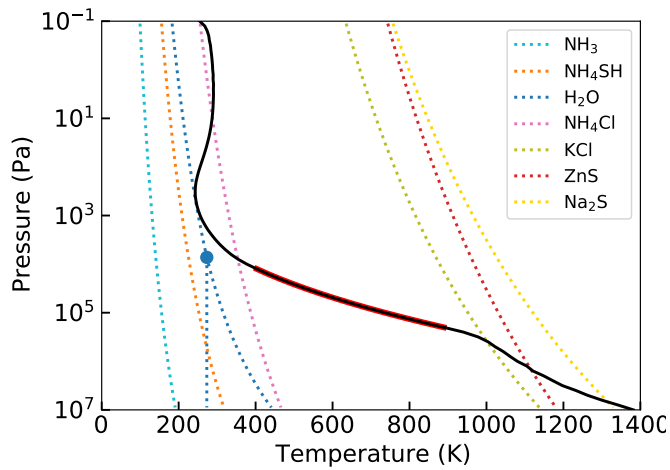


Fig. 4: Temperature profile of our best fit atmospheric model against the dataset from Benneke et al. (2019a) at nominal irradiation. Solid line: Temperature profile. Dotted lines: Condensation profiles of selected species. Red line: Convective layers. Blue dot: H<sub>2</sub>O ice-Ih-liquid-gas triple point.

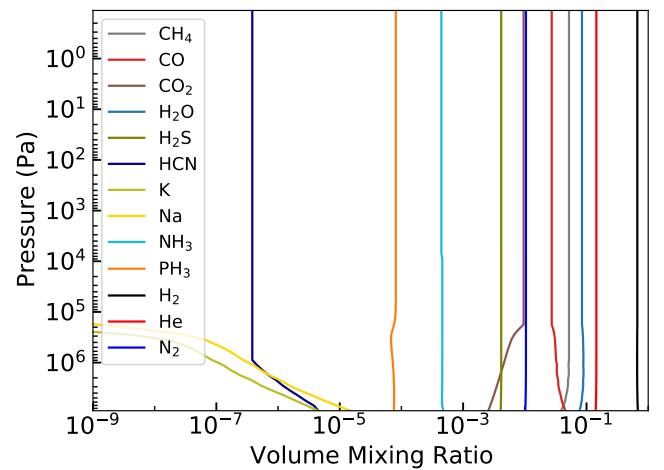


Fig. 5: VMR of our best fit atmospheric model against the dataset from Benneke et al. (2019a) at nominal irradiation ( $175 (Z/H)_{\odot}$ ,  $K_{zz} = 10^6 \text{ cm}^2 \cdot \text{s}^{-1}$ ). For clarity, only absorbing species and N<sub>2</sub> are represented. FeH, TiO, and VO are not represented as their respective abundances are, respectively,  $< 10^{-12}$ ,  $< 10^{-35}$ , and  $< 10^{-36}$  within our pressure grid. The bump of the PH<sub>3</sub> VMR at 200 kPa is due to the chemical equilibrium between PH<sub>3</sub> and P<sub>2</sub> peaking in favour of P<sub>2</sub> at this pressure.

vigorous vertical mixing alone cannot explain a CH<sub>4</sub>-depleted atmosphere.

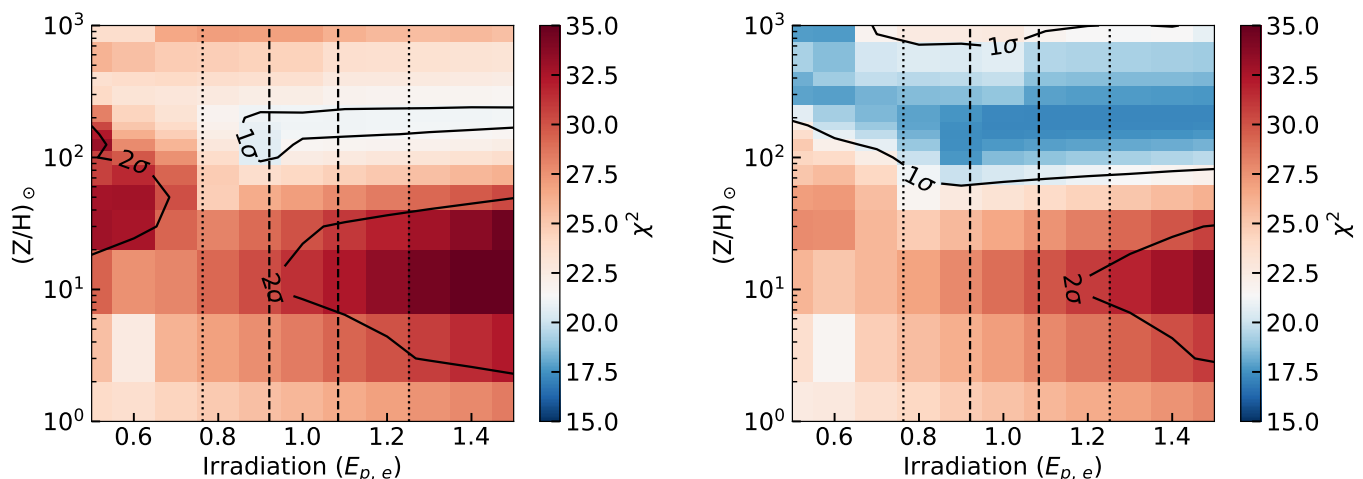


Fig. 6: Goodness of fit of our nominal models, varying only irradiation and metallicity. Left: Data from Benneke et al. (2019a), including HST, K2, and Spitzer data. Right: Data from Tsiaras et al. (2019), including HST, K2, and Spitzer data. The white colour corresponds to the value of  $\chi^2$  of 21.36, indicating a fit of the datasets at the  $1\sigma$  confidence level. Accordingly, the blue colour indicates overfit and the red colour underfit of the datasets. The solid lines represents the  $1\sigma$  and  $2\sigma$  confidence levels of our fits. The dashed and dotted lines represents, respectively, the  $1$  and  $3\sigma$  uncertainties on K2-18b irradiation.

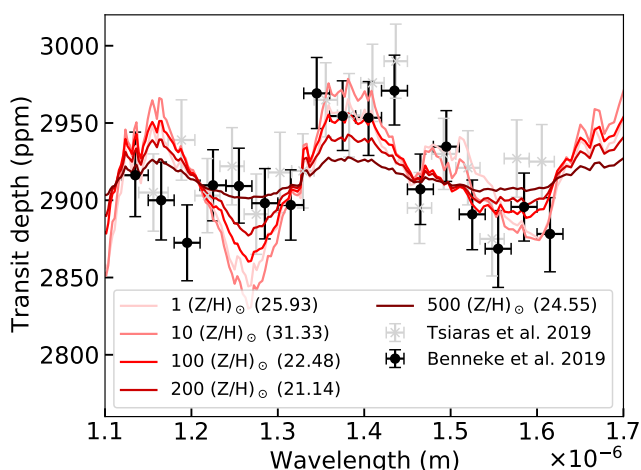


Fig. 7: Effect of metallicity on the transmission spectrum at nominal irradiation. The corresponding value of  $\chi^2$  against Benneke et al. (2019a) data is indicated in parentheses.

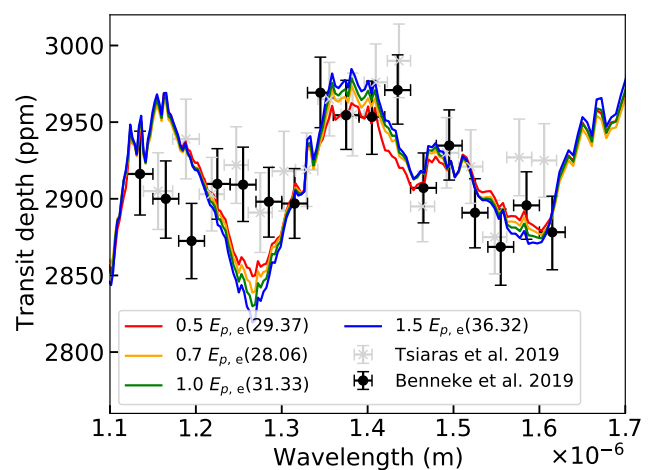


Fig. 8: Effect of irradiation on the transmission spectrum at  $10 (Z/H)_\odot$ . The corresponding value of  $\chi^2$  against Benneke et al. (2019a) data is indicated in parentheses.

#### 4.4. C/O ratio

We simulated atmospheres with 30, 50, 75, 100, 125, 150, 175, 200, 300, 400, and 500 times the solar system metallicity for all elements except C and the noble gases, and with a carbon-to-hydrogen abundance ratio (C/H) of 0.3, 1, 2, 5, 10, 30, 50, 75, 100, 150, 200, 300, 400, and 500 times the solar ratio. The  $\chi^2$  of these simulations against Benneke et al. (2019a) data are displayed in Figure 16. We call that our ‘free C/H’ scenario. Our best fit against Tsiaras et al. (2019) data ( $\chi^2 = 17.07$ ) is located at  $125 (Z/H)_\odot$  and  $50 (C/H)_\odot$  ( $C/O = 0.22^6$ ), while our best fit against Benneke et al. (2019a) data ( $\chi^2 = 18.86$ ) is located at  $125 (Z/H)_\odot$  and  $30 (C/H)_\odot$  ( $C/O = 0.13$ ). A discussion of these results is available in Section 5.2.2.

<sup>6</sup>  $(C/O)_\odot = 0.550^{+0.130}_{-0.108}$  (Lodders 2019)

## 5. Comparisons with previous studies and discussions

### 5.1. Considering whether $H_2O$ or $CH_4$ is the dominant absorber in the HST transit spectra

Our nominal model, presented in Section 4, shows that  $CH_4$  should be the main C-bearing species in the atmosphere, and, despite  $H_2O$  being more abundant than  $CH_4$ , the latter should be the main contributor to the absorption features of the transmission spectrum. In particular,  $CH_4$  and  $H_2O$  have an overlapping band at  $1.4 \mu m$  in the HST-WFC3 spectral range. This is outlined in Bézard et al. (2020), who showed that at this wavelength and for sub-Neptunes with effective temperatures lower than  $\approx 600$  K and high atmospheric metallicities,  $CH_4$  should be a stronger absorber than  $H_2O$  in transit spectroscopy due to the numerous

Table 8: Comparison of the Bayesian log-evidence of TauREx 3 against Benneke et al. (2019a) dataset for different models.

Setup	$\log(Z)$	$\chi^2$	$\log_{10}(\text{CH}_4)$	$\log_{10}(\text{H}_2\text{O})$	$\log_{10}(P_{\text{clouds}})(\text{Pa})$
No active gas <sup>a</sup>	171.03	31.78	-	-	$2.84^{+1.97}_{-1.55}$
<b>With clouds:</b>					
All absorbers <sup>b</sup>	178.83	8.63	$-7.29^{+1.74}_{-1.64}$	$-2.09^{+0.81}_{-1.06}$	$3.83^{+0.75}_{-0.53}$
No H <sub>2</sub> O <sup>c</sup>	173.22	21.34	$-2.60^{+1.23}_{-1.15}$	-	$3.04^{+1.07}_{-1.06}$
CH <sub>4</sub> -only	173.24	20.95	$-2.53^{+1.13}_{-1.31}$	-	$2.94^{+1.13}_{-0.96}$
No CH <sub>4</sub> <sup>c</sup>	178.57	8.84	-	$-2.48^{+0.94}_{-1.00}$	$3.93^{+0.73}_{-0.49}$
H <sub>2</sub> O-only	178.89	8.66	-	$-2.51^{+1.11}_{-1.14}$	$3.95^{+0.77}_{-0.61}$
<b>No cloud:</b>					
All absorbers <sup>b</sup>	177.40	10.50	$-7.55^{+1.60}_{-1.48}$	$-3.28^{+1.74}_{-0.75}$	-
CH <sub>4</sub> -only	172.20	21.12	$-1.83^{+1.20}_{-2.07}$	-	-
H <sub>2</sub> O-only	178.60	9.50	-	$-3.34^{+1.69}_{-0.79}$	-

**Notes.** All the models, except the 'no active gas' model, include H<sub>2</sub>-H<sub>2</sub> and H<sub>2</sub>-He CIA, Rayleigh scattering and N<sub>2</sub> contribution to  $\mu$ . <sup>(a)</sup> Grey cloud without molecular absorptions, CIA and Rayleigh scattering. <sup>(b)</sup> CH<sub>4</sub>, CO, CO<sub>2</sub>, H<sub>2</sub>O and NH<sub>3</sub>. <sup>(c)</sup> Same as (b), but without H<sub>2</sub>O or CH<sub>4</sub>.

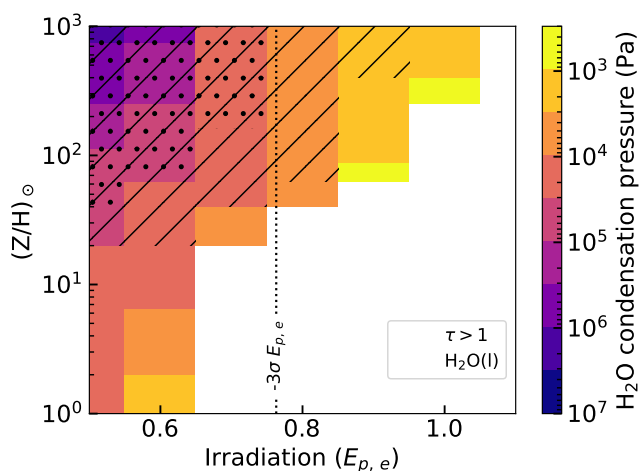


Fig. 9: H<sub>2</sub>O condensation pressure level of our nominal models, varying only irradiation and metallicity. White squares: No cloud formation. Strips: Simulation where the H<sub>2</sub>O clouds are optically thick (normal optical depth  $\tau > 1$  at  $1 \mu\text{m}$ ). Dots: Simulations where H<sub>2</sub>O condenses into its liquid phase. Dotted line:  $3\sigma$  lower limit of K2-18b irradiation.

weak lines of CH<sub>4</sub>. However, this is in disagreement with Benneke et al. (2019a) and Tsiaras et al. (2019) who claim that the HST data provide evidence for the presence of H<sub>2</sub>O.

To investigate this discrepancy, Bézard et al. (2020) compared their best fit Exo-REM spectrum (in which CH<sub>4</sub> absorption dominates over H<sub>2</sub>O) and an H<sub>2</sub>O-only spectrum (in which all other absorbers were removed) to the HST data reduced by Tsiaras et al. (2019). The  $\chi^2$  associated with the two models are essentially the same (0.91 and 0.93). In addition, applying the retrieval algorithm TauREx 3 (Al-Refaie et al. 2019) to these data, Bézard et al. (2020) found solutions favouring a CH<sub>4</sub>-rich atmosphere whose absorption at  $1.4 \mu\text{m}$  is dominated by CH<sub>4</sub>. Thus, the apparent disagreement with the analysis of Tsiaras et al. (2019) simply arises from the fact that these authors did not consider an atmosphere with significant amounts of CH<sub>4</sub> in the three scenarios they investigated.

Regarding the Benneke et al. (2019a) dataset, we used the same technique as Bézard et al. (2020): we took the H<sub>2</sub>O contri-

bution of our best-fit spectrum, displayed in Figure 3, and compared it with the data. In the same way, we made another spectrum with only the contributions of the absorbers included in the retrieval analysis of Benneke et al. (2019a) except CH<sub>4</sub> (i.e. H<sub>2</sub>O, CO, CO<sub>2</sub>, and NH<sub>3</sub>, HCN contribution is negligible and was not included). We will refer to this latter spectrum as 'no CH<sub>4</sub>'. We stress that none of these spectra are directly the results of self-consistent simulations. They are displayed in Figure 17. We found that our H<sub>2</sub>O-only spectrum does provide a superior fit compared with our best fit Exo-REM model. The fit is improved in the  $1.15\text{--}1.20 \mu\text{m}$  spectral range, around  $1.6 \mu\text{m}$ , and for the Spitzer data points. With our 'no CH<sub>4</sub>' spectrum, the fit is also better than our best-fit model, but less so than our H<sub>2</sub>O-only spectrum due to the absorptions of NH<sub>3</sub> in the HST spectral range and the CO and CO<sub>2</sub> absorptions in the Spitzer spectral range. We note that our VMRs of NH<sub>3</sub>, N<sub>2</sub>, CO, and CO<sub>2</sub> of respectively 0.04%, 1.02%, 2.73%, and 0.96% (see Figure 5), are all lower than the ' $2\sigma$  (97.5%)' upper limits given by Benneke et al. (2019a) for these species (respectively 13.5%, 10.9%, 7.45% and 2.4%). The spectrum with only H<sub>2</sub>O absorption is strongly overfitting the Benneke et al. (2019a) data, with a  $\chi^2$  of 13.01. On the other hand, our best-fit model, with a  $\chi^2$  of 21.07, is still within the  $1\text{-}\sigma$  confidence interval ( $\chi^2 < 21.36$ ). The 'no CH<sub>4</sub>' spectrum is characterised by a slight overfitting, providing a better  $\chi^2$  (18.83) compared to our best fit, but the removal of CH<sub>4</sub> absorption is artificial.

We also applied TauREx 3 to the Benneke et al. (2019a) data. This algorithm uses the nested sampling code Multinest (Feroz et al. 2009) to explore the parameter space and find the best fit corresponding to a given spectrum. In this retrieval analysis, we used 500 live points, an evidence tolerance of 0.5, and the cross-sections provided by the TauREx website<sup>7</sup> at a resolution power of 15000 and between 0.3 and  $15 \mu\text{m}$ . We simulated the atmosphere of K2-18b using an isothermal temperature profile with 100 atmospheric layers between  $10^{-3}$  and  $10^6$  Pa. We took into account molecular absorptions from CH<sub>4</sub>, CO, CO<sub>2</sub>, H<sub>2</sub>O, and NH<sub>3</sub>, CIA from H<sub>2</sub>-H<sub>2</sub> and H<sub>2</sub>-He, the contribution to  $\mu$  of N<sub>2</sub>, Rayleigh scattering and spectrally gray clouds. The planet radius was allowed to vary by  $\pm 10\%$  of its value determined by Benneke et al. (2019a), while the cloud top was allowed to be between  $10^6$  and 1 Pa. We chose to set bounds on the temperature and the species VMR, respectively, between 200 and 400 K, and between  $10^{-10}$  and 0.3. The corresponding posterior distri-

<sup>7</sup> <https://exoai.github.io/software/taurex/xsec>

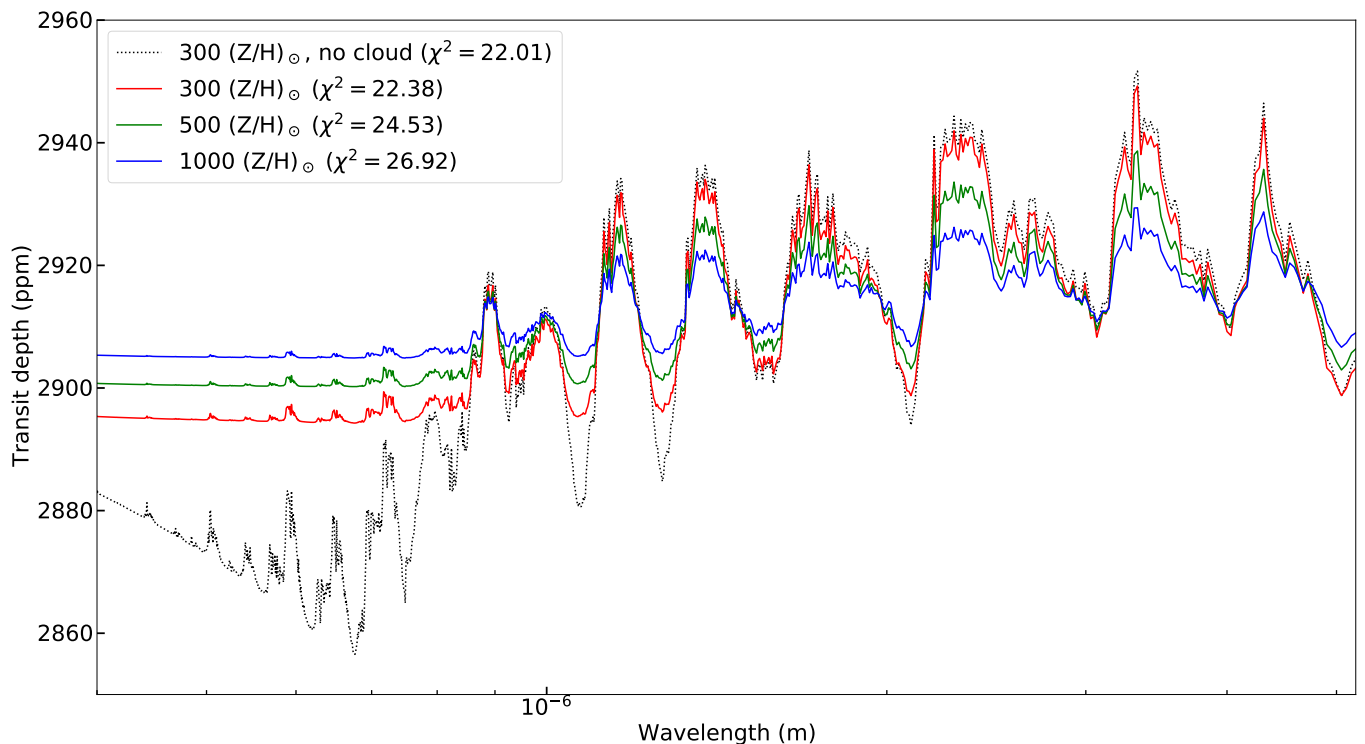


Fig. 10: H<sub>2</sub>O cloud and metallicity effect on the transmission spectrum, at nominal irradiation. The  $\chi^2$  against Benneke et al. (2019a) data is indicated in parentheses.

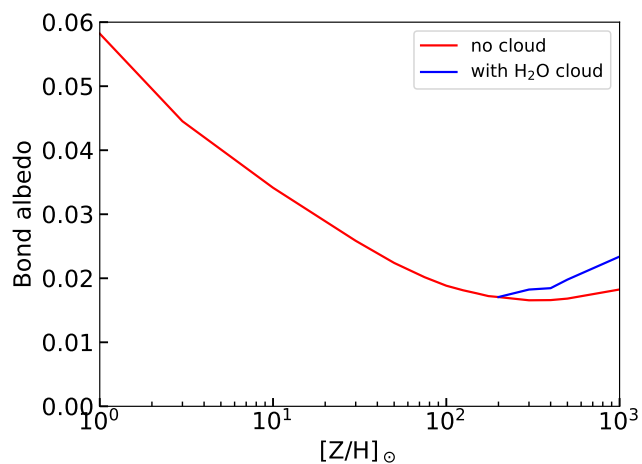


Fig. 11: H<sub>2</sub>O cloud and metallicity effect on the Bond albedo of K2-18b, at nominal irradiation. Cloud condensation occurs only above 200 (Z/H)<sub>sun</sub>.

contributions are shown in Figure 18. We also tested models removing all molecular absorptions except H<sub>2</sub>O or CH<sub>4</sub>, removing clouds, or including all absorptions except that of H<sub>2</sub>O. For comparison, we also computed a ‘no active gas’ model including only the cloud contribution, that is, a flat spectrum. Finally, we calculated the  $\chi^2$  and corresponding  $\sigma$  confidence of each model using the same technique as in Section 4 and the ‘binned’ spectrum output from TauREx 3. Our results are summarised in Table 8. A small discussion on the results is available in Appendix B.

We found that solutions with low amounts of CH<sub>4</sub> are unambiguously favoured: the ‘all absorbers with clouds’ model we used is favoured over the ‘no H<sub>2</sub>O with clouds’ model at 273:1 ( $3.79\sigma$ , see Benneke & Seager 2013). The difference in log-evidence between our CH<sub>4</sub>-only models and our ‘H<sub>2</sub>O-included’ models (i.e. all models including at least the molecular absorption of H<sub>2</sub>O) is, at worst of 4.16, indicating that the latter are favoured at  $\geq 64:1$  ( $3.35\sigma$ ). Moreover, the  $2\sigma$  (95.4%) upper limit of CH<sub>4</sub> is 0.009% with our ‘all absorbers with clouds’ model, even lower than what was inferred by Benneke et al. (2019a) (0.248%). This confirms that an H<sub>2</sub>O-dominated spectrum is a far better fit to the Benneke et al. (2019a) dataset than a CH<sub>4</sub>-dominated spectrum, but not that the latter must be rejected. Indeed, looking at the  $\chi^2$ , we find that all of the spectra obtained from our TauREx 3 models that do not include H<sub>2</sub>O are slightly below the  $1\sigma$  confidence level, with  $\chi^2$  values and CH<sub>4</sub> VMR close to our Exo-REM best fit. In contrast, all the H<sub>2</sub>O-included TauREx 3 spectra strongly overfit the spectrum, with  $\chi^2 \leq 10.50$ , which is much less than the number of data points, and likely much less than the number of effective degrees of freedom. We interpret this as an H<sub>2</sub>O-only spectrum leading to a significant overfit of the dataset.

The overfit that we identified could be explained by an overestimation of the HST error bars. However, the Benneke et al. (2019a) and Tsiaras et al. (2019) HST spectra that we analysed come from independent reduction methods (Tsiaras et al. 2018) and both show similar transit depth uncertainties. Moreover, the custom HST pipeline used by Tsiaras et al. (2019) is described in Tsiaras et al. (2018) to exhibit ‘nearly photon-noise limited’ performance, meaning that the spectral uncertainties should be close to the theoretical minimum. It can also be seen, for example, in Figure 7 that the data points near 1.2  $\mu\text{m}$  from the two datasets

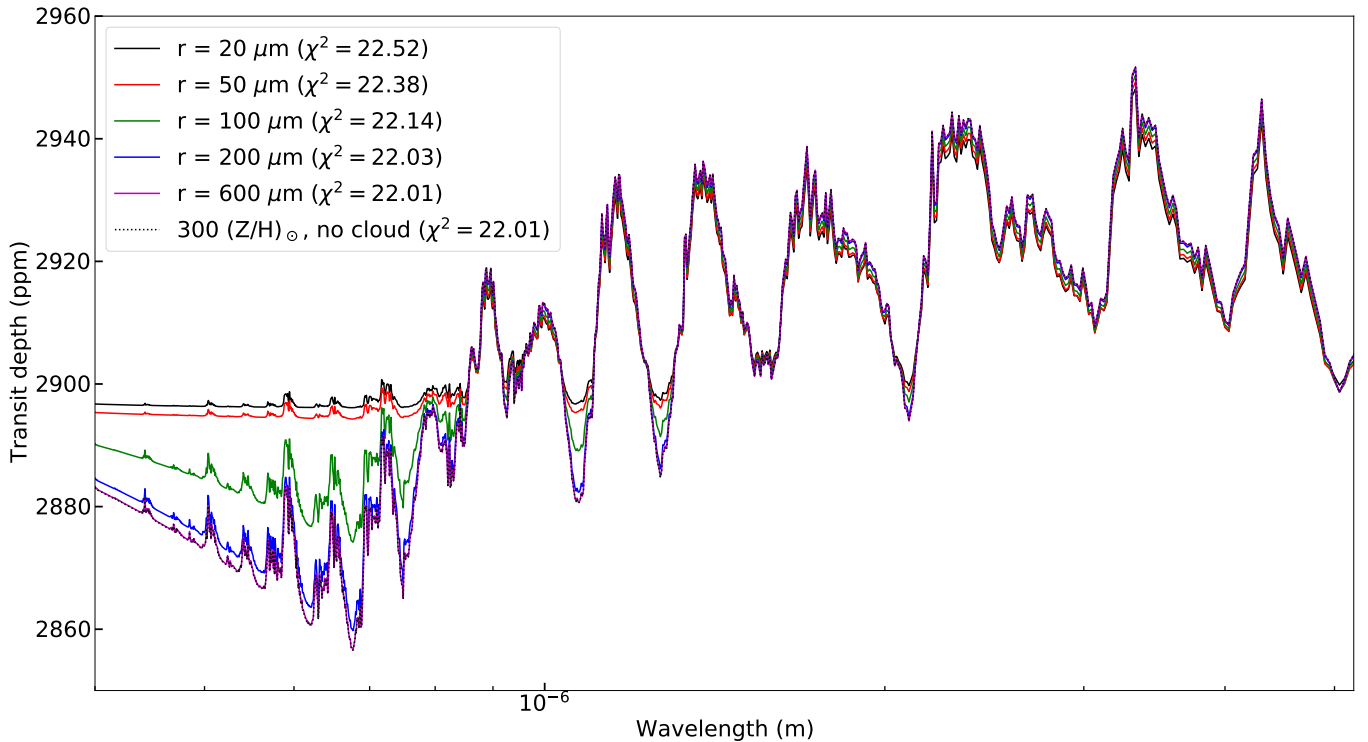


Fig. 12: H<sub>2</sub>O cloud particle radius effect on the transmission spectrum, at 300 (Z/H)<sub>⊙</sub> and at nominal irradiation. The  $\chi^2$  against Benneke et al. (2019a) data is indicated in parentheses.

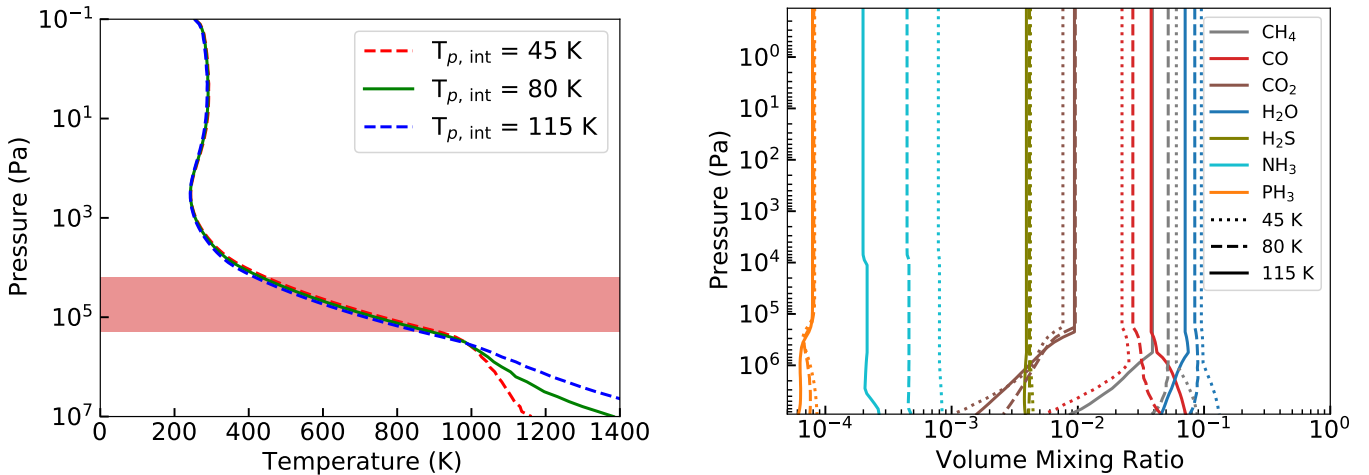


Fig. 13: Effects of  $T_{p,int}$  on K2-18b, at 175 (Z/H)<sub>⊙</sub>, nominal irradiation, and  $K_{zz} = 10^6 \text{ cm}^2 \cdot \text{s}^{-1}$ . Left: Temperature profiles. The red area represents the convective layers. Right: VMR of the most abundant absorbers. Dotted:  $T_{p,int} = 45 \text{ K}$ . Dashed:  $T_{p,int} = 80 \text{ K}$ . Solid:  $T_{p,int} = 115 \text{ K}$ .

are not compatible at the 1- $\sigma$  confidence level, which points to additional systematic errors. These are probably linked to uncertainties in some parameters used in the data reduction (orbital parameters, limb-darkening coefficients, or calibration, as suggested in Tsiaras et al. 2018). For all of these reasons, we regard this possibility as unlikely.

To summarise, of the two datasets available to us, only the one from Benneke et al. (2019a) strongly favours a CH<sub>4</sub>-depleted atmosphere. This favouritism is likely due to free retrieval algo-

gorithms searching for the solution that best fits the data. But if such a solution is strongly overfitting, as is the case for an H<sub>2</sub>O-only spectrum against the dataset from Benneke et al. (2019a), any other solution that is considered to be more physically acceptable may also appear as statistically unlikely. However, if a strong depletion of CH<sub>4</sub> in the atmosphere of K2-18b is not a straightforward scenario from a chemical standpoint and ends up overfitting the data, it is indisputably a statistically valid one

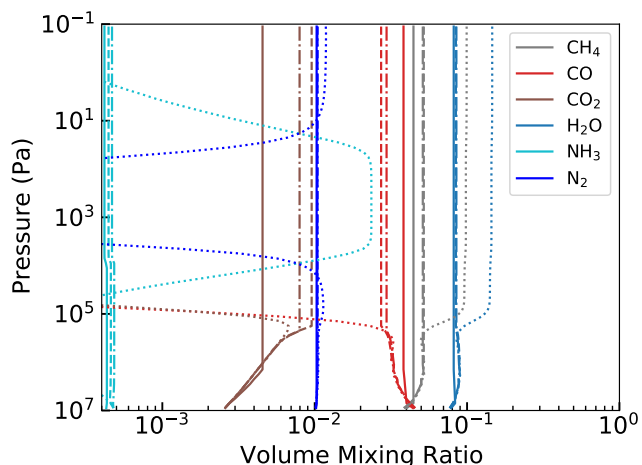


Fig. 14: Effects of  $K_{zz}$  on the VMR of K2-18b main C, N, O bearing species, at 175  $(Z/H)_\odot$ . Dashed:  $K_{zz} = 10^6 \text{ cm}^2 \cdot \text{s}^{-1}$ . Dotted-dashed:  $K_{zz} = 10^8 \text{ cm}^2 \cdot \text{s}^{-1}$ . Solid:  $K_{zz} = 10^{10} \text{ cm}^2 \cdot \text{s}^{-1}$ . Dotted: Thermochemical equilibrium.

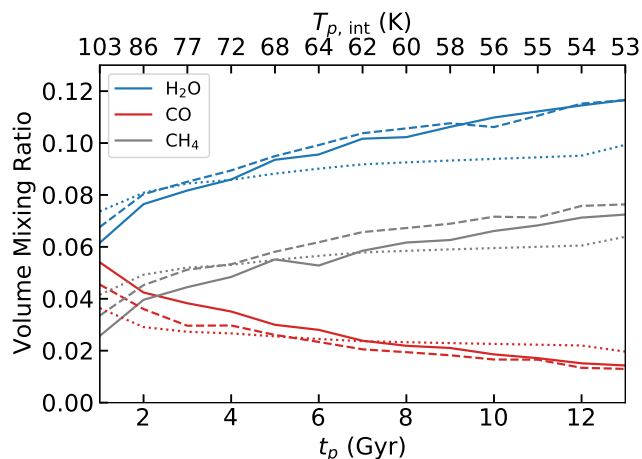


Fig. 15: Chemical evolution of the upper atmosphere of K2-18b for the most abundant C- and O-bearing species over time, depending on the value of  $K_{zz}$ , at 175  $(Z/H)_\odot$ . Dotted:  $K_{zz} = 10^6 \text{ cm}^2 \cdot \text{s}^{-1}$ . Dashed:  $K_{zz} = 10^8 \text{ cm}^2 \cdot \text{s}^{-1}$ . Solid:  $K_{zz} = 10^{10} \text{ cm}^2 \cdot \text{s}^{-1}$ .

and, thus, it must be considered. In the next section, we try to find a model that could explain such a depletion.

## 5.2. $\text{CH}_4$ -depleted scenarios for K2-18b

While our standard models, presented in Section 4, are statistically able to reproduce the observed spectrum of K2-18b, here we test some scenarios allowing for  $\text{CH}_4$  VMR to be as small as retrieved by all the other teams who analysed the data so far. Indeed, our nominal model gives a  $\text{CH}_4$  VMR of  $\approx 5_{-2}^{+1}\%$  (for metallicities between 65 and 500  $(Z/H)_\odot$ ), while Benneke et al. (2019a), Madhusudhan et al. (2020) and Scheucher et al. (2020) give, respectively, a  $2\sigma$  upper limit of 0.248%, a 99% upper limit of 3.47%, and an upper limit of 460 ppm. Benneke et al. (2019b) propose three explanations to this depletion: (i) a high internal temperature, either from residual heat of formation or tidal heat-

ing, (ii) a low C/O ratio resulting from planetary formation process, and (iii) a catalytic destruction of  $\text{CH}_4$  by photolysis. The latter cannot be simulated using Exo-REM, so we will focus on the first two possibilities.

### 5.2.1. High internal temperature

Following the trend presented in Section 4.3, it is possible to reach a  $\text{CH}_4$  VMR that is compatible with what was found by Benneke et al. (2019a) by considering  $T_{p,\text{int}}$  as high as 200 K. Using this internal temperature, we simulated atmospheres at 30, 50, 75, 100, 125, 150, 175, 200, 300, 400, and 500  $(Z/H)_\odot$  and within our selected range of  $K_{zz}$ . The goodness of fit for our models compared to the datasets from Benneke et al. (2019a) and Tsiaras et al. (2019) is displayed in Figure 19. We note that  $\text{H}_2\text{O}$  never dominates the transmission spectrum in the 1.355–1.415  $\mu\text{m}$  window. Our best fit against Tsiaras et al. (2019) data ( $\chi^2 = 16.78$ ) is located at 150  $(Z/H)_\odot$  and  $10^7 \text{ cm}^2 \cdot \text{s}^{-1}$ , while our best fit against Benneke et al. (2019a) data ( $\chi^2 = 20.70$ ) is located at 150  $(Z/H)_\odot$  and  $10^{10} \text{ cm}^2 \cdot \text{s}^{-1}$ . There is no  $\text{H}_2\text{O}$  cloud condensation in the latter scenario. The goodness of fit is again slightly better than for our nominal model. The VMR are displayed in Figure 20. In this configuration, we obtain VMR for  $\text{CH}_4$ ,  $\text{CO}$ ,  $\text{CO}_2$ ,  $\text{NH}_3$ , and  $\text{H}_2\text{O}$  in the upper atmosphere at levels of 0.283%, 6.589%, 0.280%, 0.006%, and 1.657%, respectively, which are all below or close to the  $2\sigma$  upper limit found by Benneke et al. (2019a).

Reaching such a high internal temperature, however, would require K2-18b to be a very young planet ( $\ll 1$  Gyr old according to Equation 2) or a planet experiencing strong tidal heating, or both. According to the internal temperature model we used and the age of the system determined by Guinan & Engle (2019), it seems unlikely that the residual heat of formation could be sufficient to explain a high internal temperature. To assess the possibility of strong tidal heating on K2-18b, we can make a few considerations. The K2-18 system is composed of at least another planet: K2-18 c (Cloutier et al. 2019), orbiting closer to its star than K2-18b. Both planets may have a moderately high eccentricity that is rapidly evolving due to the secular interactions between the two objects (Gomes & Ferraz-Mello 2020). In that configuration, a lot of orbital energy can indeed be dissipated, but only in the innermost planet<sup>8</sup>, that is, K2-18 c. Thus, there should be no tidal heating on K2-18b.

### 5.2.2. Low C/O

To test the possibility of a low atmospheric C/O ratio on K2-18b, we use the results from the simulations presented in Section 4.4. The VMR of the most abundant absorbers in our best fit against Benneke et al. (2019a) are represented in Figure 21. The amount of  $\text{CH}_4$  in the upper atmosphere we obtain in this best-fit simulation is 1.23%, incompatible with the  $2\sigma$  upper limit found by Benneke et al. (2019a) (0.248%), but compatible with the 99% upper limit found by Madhusudhan et al. (2020) (3.47%). However, simulations at metallicities between 50 and 150  $(Z/H)_\odot$  at 5  $(C/H)_\odot$  and at 20  $(Z/H)_\odot$  and 1  $(C/H)_\odot$  are statistically able to reproduce the data while allowing the  $\text{CH}_4$  VMR to be close or below 0.248%, with a minimum at 0.101%. There is no simulation within the  $1\sigma$  confidence level for  $C/H \lesssim 1$   $(C/H)_\odot$  ( $\text{CH}_4$  VMR  $\lesssim 0.05\%$  at 50  $(Z/H)_\odot$ ). Accordingly, C/O must be  $\gtrsim 0.01$  (0.02  $(C/O)_\odot$ ) in order to obtain a satisfactory fit of the data. We note that C/H must be  $\lesssim 5$   $(C/H)_\odot$  (or  $C/O \lesssim 0.1$   $(C/O)_\odot$ ) in order for

<sup>8</sup> J. Leconte, private communication.

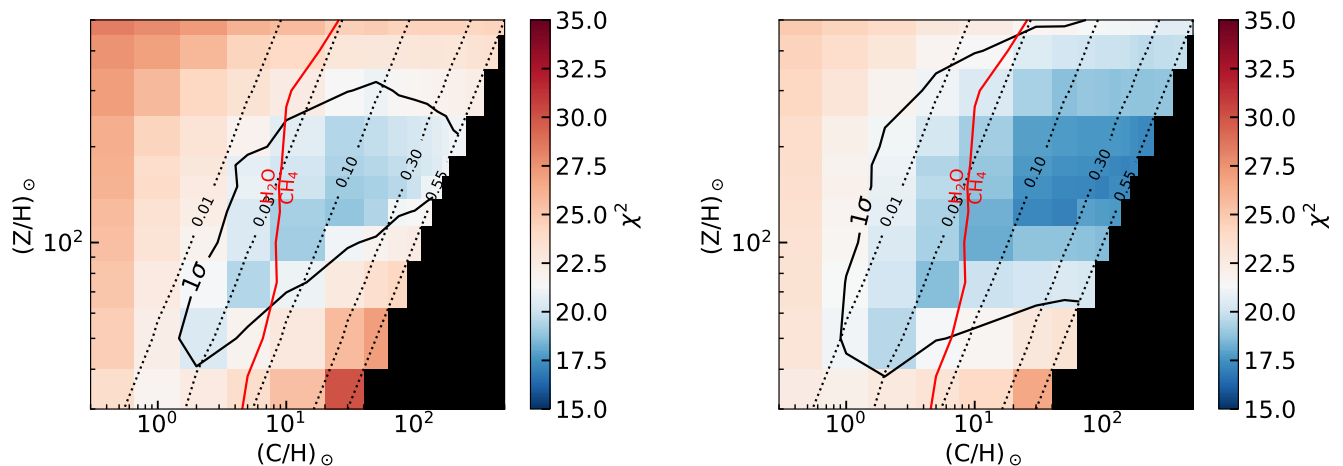


Fig. 16: Goodness of fit of our models for  $T_{p,int} = 80$  K,  $K_{zz} = 10^6$   $\text{cm}^2\cdot\text{s}^{-1}$  and nominal irradiation, as a function of the metallicity and C/H, compared to the data from Benneke et al. (2019a) (left) and Tsiaras et al. (2019) (right). The white colour corresponds to the value of  $\chi^2 = 21.36$ , indicating a fit at the  $1\sigma$  confidence level. The solid black line represents the  $1\sigma$  confidence level. The dotted lines indicates the C/O ratio. The solid red line indicates which species dominates on average the transmission spectrum in the 1.355–1.415  $\mu\text{m}$  range. The cases where  $\text{C/O} > (\text{C/O})_{\odot}$  was not explored are represented as black rectangles.

$\text{H}_2\text{O}$  to dominate the transmission spectrum in the 1.355–1.415  $\mu\text{m}$  interval.

Heavily C-depleted atmospheres ( $\text{C/O} \lesssim 0.01$ ) do not seem to agree with the data. Lowering the abundance of C in the atmosphere naturally decreases the contribution of  $\text{CH}_4$  to the transmission spectrum, and improves the fit of Benneke et al. (2019a) data, as discussed in Section 5.2. A side effect, however, is that because  $\text{CH}_4$  has a strong greenhouse effect, the temperatures decrease significantly, favouring the condensation of  $\text{H}_2\text{O}$ , dampening the absorption features of the latter, and worsening the fit around 1.4  $\mu\text{m}$ . This side effect explains why our results are quite different from the results of other teams who used free retrieval algorithms that do not include any physical constraint on the model atmosphere. Moderately-C-depleted atmospheres ( $\text{C/O} \approx 0.10$ ), on the contrary, are clearly favoured, but in that case  $\text{CH}_4$  still dominates the absorption features of the transmission spectrum. Moreover, the precise phenomenon that could lead to such a depletion has, to our knowledge, yet to be discovered.

## 6. Observational perspectives

For K2-18b, acquiring higher resolution spectra would permit to discriminate between the three scenarios we identified. We used our  $0.5 \text{ cm}^{-1}$  resolution  $k$ -coefficient set to derive high-resolution spectra of K2-18b and show some spectral ranges in Figure 22 that could prove interesting in that regard. We note that  $\text{NH}_3$  dominates the 1.45–1.56  $\mu\text{m}$  spectral range for any of the following three scenarios.

Firstly, in the nominal scenario,  $\text{CH}_4$  should dominate over most of the infrared (IR) transmission spectrum, with particularly strong lines around 1.6  $\mu\text{m}$  (end of the H band), or in the 3.0–4.0  $\mu\text{m}$  spectral range (L band).  $\text{CO}$  would dominate the spectrum in the 4.6–5.0  $\mu\text{m}$  spectral range (M band) but not in the 2.3–2.5  $\mu\text{m}$  spectral range (end of the K band). Isolating  $\text{H}_2\text{O}$  lines would be challenging in the IR, but might be possible around 1.16  $\mu\text{m}$  and 1.37  $\mu\text{m}$  (beginning and end of the J band). However, it should dominate around 823 and 924 nm.

Secondly, in the low C/O scenario, contrary to the nominal scenario,  $\text{H}_2\text{O}$  should overall dominate the IR spectrum over  $\text{CH}_4$ .  $\text{CH}_4$  may still dominate the spectrum at the end of the H band (1.6–1.8  $\mu\text{m}$ ), and in the K and L bands, depending on the intensity of the C-depletion. However, in contrast to the nominal scenario, it should have a minor contribution in the J band.  $\text{CO}$  might still dominate the M band, again depending on the extent of the C-depletion.

Thirdly, in the scenario involving high internal temperature or incomplete chemistry,  $\text{H}_2\text{O}$  should again dominate most of the IR spectrum.  $\text{CO}$  should dominate in the M band and possibly even in the K band, in contrast to the low C/O scenario. The  $\text{CH}_4$  spectral contribution should be similar to the low C/O scenario.

The James Webb Telescope (JWST) and the Atmospheric Remote-sensing Infrared Exoplanet Large-survey (ARIEL) mission, with their broader spectral range and precision higher than the data we studied here, will probably be very helpful to discriminate between these scenarios. In complement, we could acquire higher resolution spectra from ground-based instruments – such as the Cryogenic InfraRed Echelle Spectrograph+ (CRIRES+) or the Echelle Spectrograph for Rocky Exoplanets and Stable Spectroscopic Observations (ESPRESSO) mounted on the Very Large Telescope (VLT) – or by using the incoming generation of large telescopes (Extremely Large Telescope, Thirty Meter Telescope, etc.) in order to detect the absorption of individual lines and, thus, to unambiguously detect species.

As an example, we calculated the signal to noise ratio (S/N) we could obtain for a detection of  $\text{CH}_4$  in our nominal case using CRIRES+ at a resolution power of 100 000 in the 1.5–1.8  $\mu\text{m}$  spectral range. This spectral range has the advantage of presenting a lot of deep  $\text{CH}_4$  lines (50–100 ppm) in a band for which CRIRES+ has a high sensitivity<sup>9</sup>. We calculated a synthetic transmission spectrum at a resolving power of 100 000 using a line-by-line radiative transfer program, including absorption from  $\text{H}_2$ - $\text{H}_2$  and  $\text{H}_2\text{O}$ - $\text{H}_2\text{O}$  CIA and lines from  $\text{H}_2\text{O}$ ,  $\text{CH}_4$ ,  $\text{NH}_3$  and  $\text{CO}$ . We calculated the S/N, while neglecting the ter-

<sup>9</sup> [eso.org](http://eso.org).

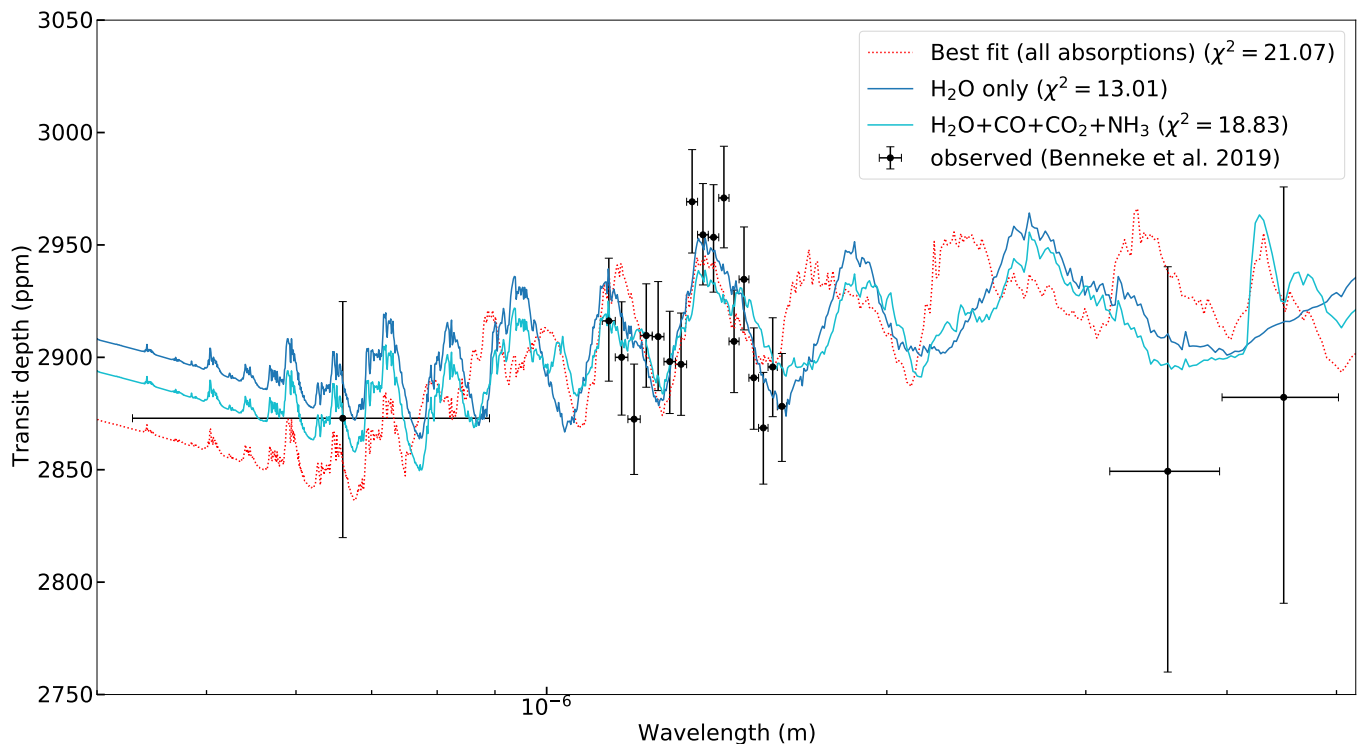


Fig. 17: Best fit against Benneke et al. (2019a) dataset with transit spectra in which the spectral contributions of selected species has been removed. Blue: H<sub>2</sub>O contribution of the transit spectrum displayed in Figure 3, with an offset of the 10<sup>5</sup>-Pa level of +98 km. Cyan: H<sub>2</sub>O, CO, CO<sub>2</sub>, and NH<sub>3</sub> total contribution of the transit spectrum displayed in Figure 3, with an offset of the 10<sup>5</sup>-Pa level of +57 km. Black: K2, HST and Spitzer from Benneke et al. (2019a). The dotted red line is our best-fit spectrum with all absorptions (see Section 4). The  $\chi^2$  of these spectra against the data is indicated in parentheses.

restrial absorptions and the photon noise of the star, using the following:

$$S/N_{\text{CH}_4} = \left( \frac{\sum_{\lambda=\lambda_{\min}}^{\lambda_{\max}} (\delta_{\text{CH}_4} - \bar{\delta}_{\text{CH}_4}) (\delta_{\text{tot}} - \bar{\delta}_{\text{tot}})}{N} \right)^{1/2} S/N_* \quad (5)$$

where  $\lambda$  is the discretised wavelength,  $\lambda_{\min}$  and  $\lambda_{\max}$  are respectively the minimum and maximum wavelengths of the considered spectral range,  $\delta_{\text{CH}_4}$  and  $\delta_{\text{tot}}$  are, respectively, the transit depths that consider only the absorption from CH<sub>4</sub> and the absorption from all absorbers; the bar indicates a smoothing by a boxcar of width 16 resolution elements (also used by Brogi et al. 2016, for their CRRES observation of HD 189733),  $N$  is the number of calculated points per resolution element within the spectral range, and  $S/N_*$  is the expected CRRES+ S/N on K2-18 for one hour of observation at  $R = 100\,000$ . From the H limiting magnitude given in eso.org, we derive a S/N of 2500 for K2-18 at  $R = 50\,000$  per spectral dispersion element for a 1-hr integration. At  $R = 100\,000$ , assuming no loss of the star signal, the S/N should thus be  $2500/\sqrt{2} = 1800$ . Hence, we can obtain a total CH<sub>4</sub> signal of 1500 ppm and, thus, from Equation 5, we have an optimistic value for  $S/N_{\text{CH}_4}$  of  $\approx 2.7$  for one hour of observation with CRRES+ at  $R = 100\,000$ . We note that the transit duration of K2-18b is approximately three hours. A full transit would give  $S/N_{\text{CH}_4} \approx 4.7$ , which is sufficient for detecting CH<sub>4</sub>. However, this estimate is probably optimistic as we did not take into account the telluric absorption and the photon noise from the star.

Observing CO from the ground would, on the other hand, prove to be extremely difficult. Even at  $R = 100\,000$ , the CO

lines overlap with those of the star. The Doppler shift between the planet and the star during the transit is in the range  $\pm 0.7$  km·s<sup>-1</sup>, which is too low to use a cross-correlation method as described by, for example, Snellen et al. (2010).

## 7. Summary and conclusions

We analysed the transmission spectrum of K2-18b between 0.43 and 5.02  $\mu\text{m}$  using a combination of K2, HST, and Spitzer data retrieved from Benneke et al. (2019a) and Tsiaras et al. (2019). We studied the effect of irradiation, metallicity, clouds, internal temperature, eddy diffusion coefficient, and C/O ratio using our self-consistent model Exo-REM and assuming an atmosphere primarily composed of H<sub>2</sub> and He. We also analysed the Benneke et al. (2019a) dataset with the retrieval algorithm TauREx 3, and provided a S/N estimation for the detection of CH<sub>4</sub> using CRRES+.

We found that the data are compatible with a highly metal-enriched atmosphere, between 65 and 500 (Z/H)<sub>⊙</sub> against Tsiaras et al. (2019) data – or between 100 and 200 (Z/H)<sub>⊙</sub> against Benneke et al. (2019a) data – when assuming a solar C/O ratio, and  $\approx 40$  (Z/H)<sub>⊙</sub> when assuming a sub-solar C/O ratio. According to our results, the atmosphere of K2-18b appears quite similar to that of Neptune or Uranus and seems to follow the C/H-mass relationship of the giant planets of our solar system, as shown in Figure 23. Most of the extrasolar planets seem to have an O/H ratio below that expected from the C/H-mass relationship for solar-system giant planets. Part of the explanation could reside in the fact that for most of these planets, the amount of CO and CO<sub>2</sub>

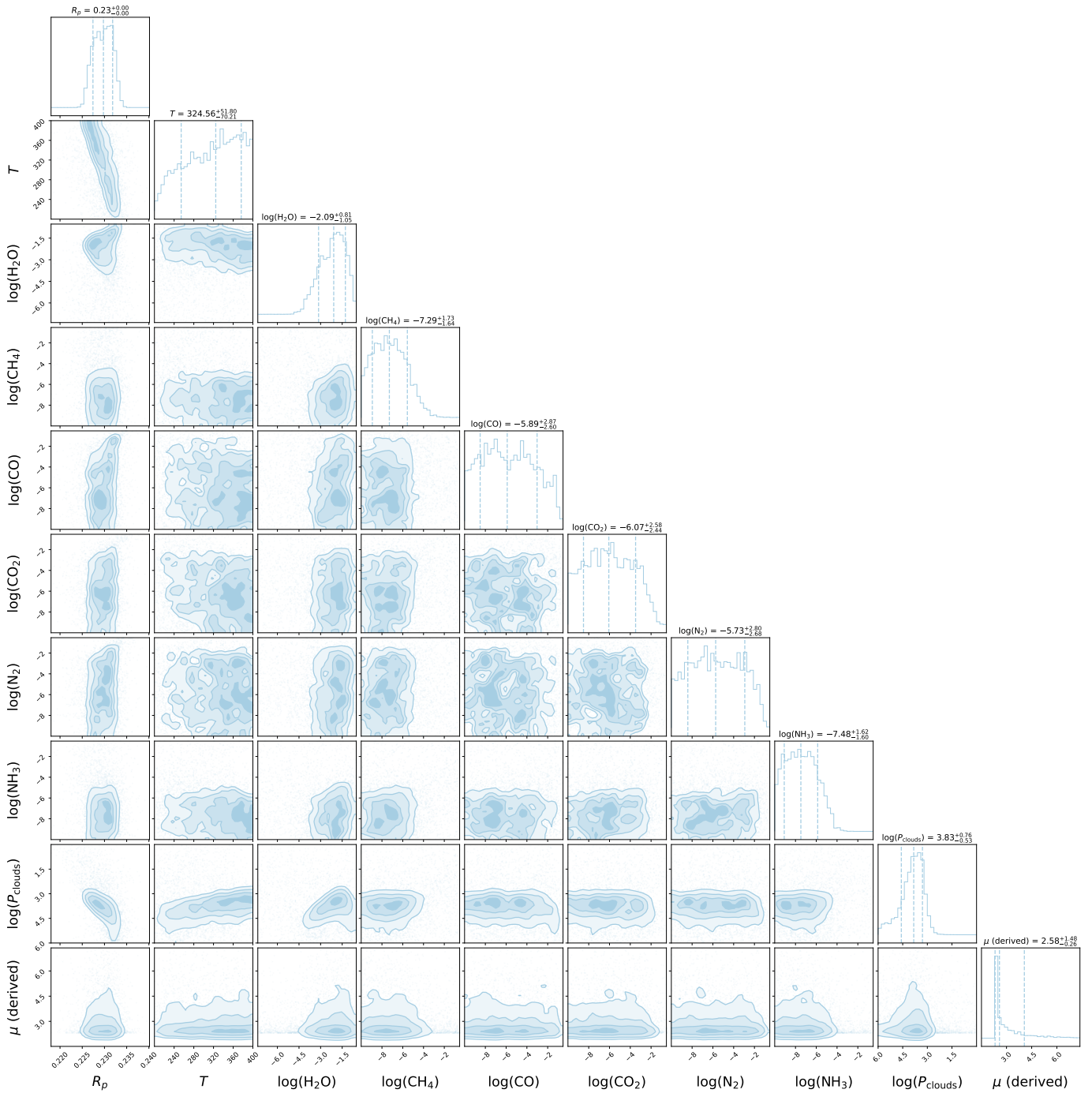


Fig. 18: TauREx 3 atmospheric retrieval posterior distributions against the dataset from [Benneke et al. \(2019a\)](#), with planetary radius ( $R_p$ ), temperature (K), decimal logarithm of the VMR of H<sub>2</sub>O, CH<sub>4</sub>, CO, CO<sub>2</sub>, N<sub>2</sub>, and NH<sub>3</sub>, and decimal logarithm of the cloud top pressure (Pa) as free parameters.

is unknown, leading to an underestimation of the O/H ratio (as pointed out by e.g. [Wakeford et al. 2017](#); [Welbanks et al. 2019](#)). A summary of our results and results of other teams is displayed in [Figure 24](#), and the spectra of our best fit for each of the explored scenarios are displayed in [Figure 25](#).

We also show that thick to no H<sub>2</sub>O-ice clouds are allowed by the data. Liquid H<sub>2</sub>O clouds are possible on planets similar to K2-18b but receiving at most 80% of its irradiation. With or without clouds, we found that the Bond albedo of the planet should be around 0.02. The other studied parameters are not well constrained by the data. We note that in most of the cases we

studied, CH<sub>4</sub> absorption should dominate or be on par with that of H<sub>2</sub>O in the HST spectral window, as first outlined by [Bézard et al. \(2020\)](#).

Combining the work of [Bézard et al. \(2020\)](#) and our own retrievals using TauREx 3, we show that the discrepancy between our self-consistent results and the results from retrieval algorithms can be explained by either the discarding of CH<sub>4</sub> absorptions, as in the case of the [Tsiaras et al. \(2019\)](#) dataset, or a strong overfitting of the data, as in the case of the [Benneke et al. \(2019a\)](#) dataset.

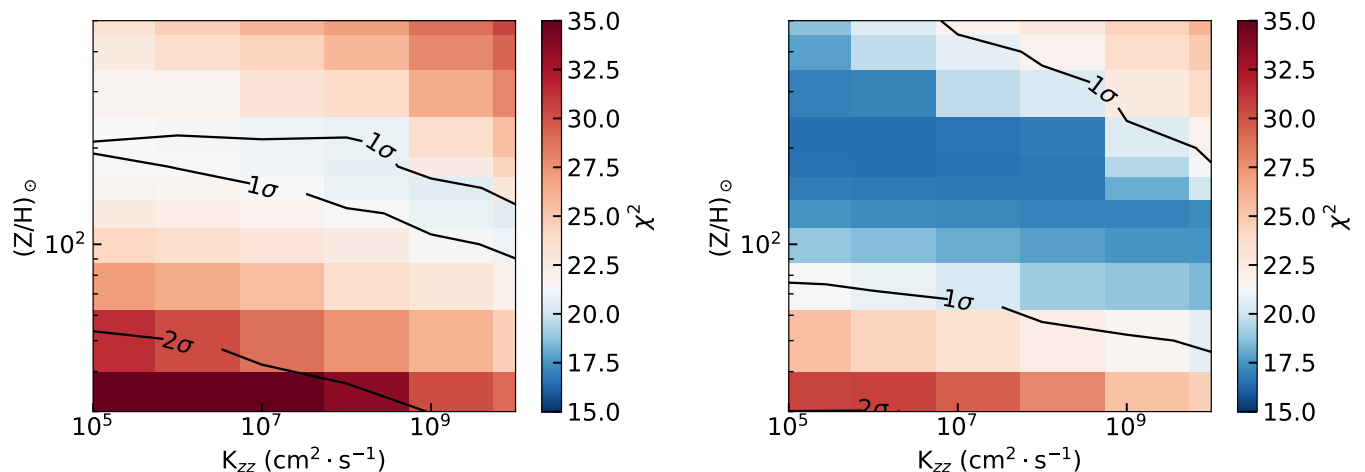


Fig. 19: Goodness of fit of our models at  $T_{p,int} = 200$  K and nominal irradiation as a function of metallicity and  $K_{zz}$ , compared to the data from [Benneke et al. \(2019a\)](#) (left) and [Tsiaras et al. \(2019\)](#) (right). The white colour corresponds to the value of  $\chi^2 = 21.36$ , indicating a fit at the  $1\sigma$  confidence level. The best fit against [Benneke et al. \(2019a\)](#) data ( $\chi^2 = 20.64$ ) is located at  $(Z/H)_{\odot} = 125$  and  $K_{zz} = 10^{10} \text{ cm}^2 \cdot \text{s}^{-1}$ . The best fit against [Tsiaras et al. \(2019\)](#) data ( $\chi^2 = 16.56$ ) is located at  $(Z/H)_{\odot} = 200$  and  $K_{zz} = 10^5 \text{ cm}^2 \cdot \text{s}^{-1}$ .

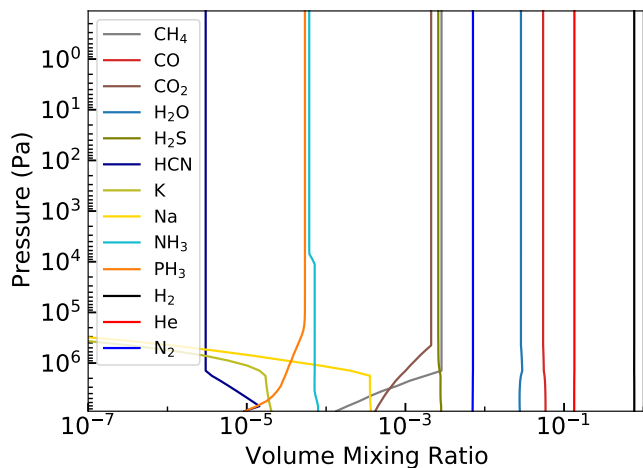


Fig. 20: VMR of selected species of our best-fit model against [Benneke et al. \(2019a\)](#) data at  $T_{p,int} = 200$  K and nominal irradiation.

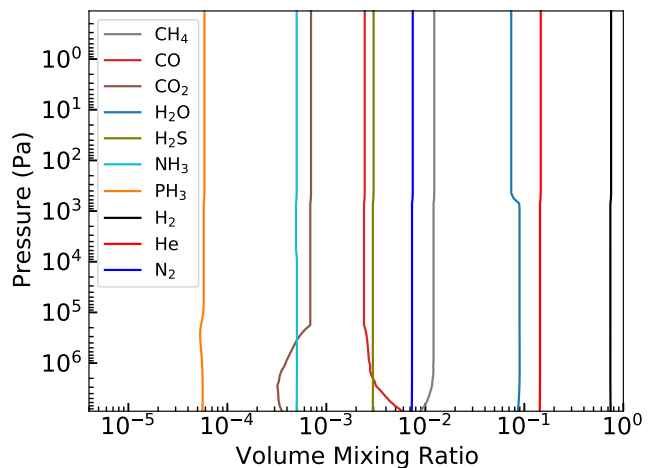


Fig. 21: VMR of selected species at  $T_{p,int} = 80$  K,  $K_{zz} = 10^6 \text{ cm}^2 \cdot \text{s}^{-1}$ , nominal irradiation,  $125 (Z/H)_{\odot}$ , and  $30 (C/H)_{\odot}$ .

Accordingly, in addition to our nominal scenario (i.e.  $Z/H = 65\text{--}500 (Z/H)_{\odot}$  and a solar  $C/O$ ), scenarios with a  $\text{CH}_4$ -depleted atmosphere could satisfactorily fit the observed spectrum. These could be obtained with a high internal temperature ( $\approx 200$  K) or a low  $C/O$  ratio ( $\gtrsim 0.01$ ), with  $\text{H}_2\text{O}$  being the dominant absorber in HST/WFC3 spectral band if  $C/O \lesssim 0.1$ . However, the high internal temperature scenario seems very unlikely, and the C-depleted scenario requires the existence of an unknown process. Therefore, it seems that a  $\text{CH}_4$ -depleted atmosphere, a scenario favoured by all other teams who have analysed the same data so far, is more difficult to defend than a nominal scenario with a standard abundance of  $\text{CH}_4$ . Moreover, a spectrum dominated by  $\text{H}_2\text{O}$  absorptions seems even more unlikely given the relatively small range of self-consistent solutions allowing for this scenario and the fact that it is favoured by retrieval algorithms only because of overfitting. Another possibility is that our thermochem-

ical model does not accurately describe the chemical conversion between  $\text{CO}$  and  $\text{CH}_4$  in the deep atmosphere, as suggested by [Benneke et al. \(2019b\)](#) in their atmospheric analysis of GJ3470b (noting that GJ3470b is a much warmer planet with an effective temperature of  $\approx 800$  K). It should be possible to discriminate between these scenarios by acquiring data in different spectral ranges and/or at higher resolution using the incoming JWST and ARIEL space telescopes. In complement, ground-based instruments such as CRIRES+ could be used to detect individual lines of species. We estimate that with our nominal scenario, we could detect  $\text{CH}_4$  with CRIRES+ in the H band with an 'optimistic' S/N of 4.7 after three hours of transit observation.

This study highlights the critical need for more precise spectroscopic data on sub-Neptunes. This will allow us to better characterise these intriguing bodies, which have no analogue in our Solar System.

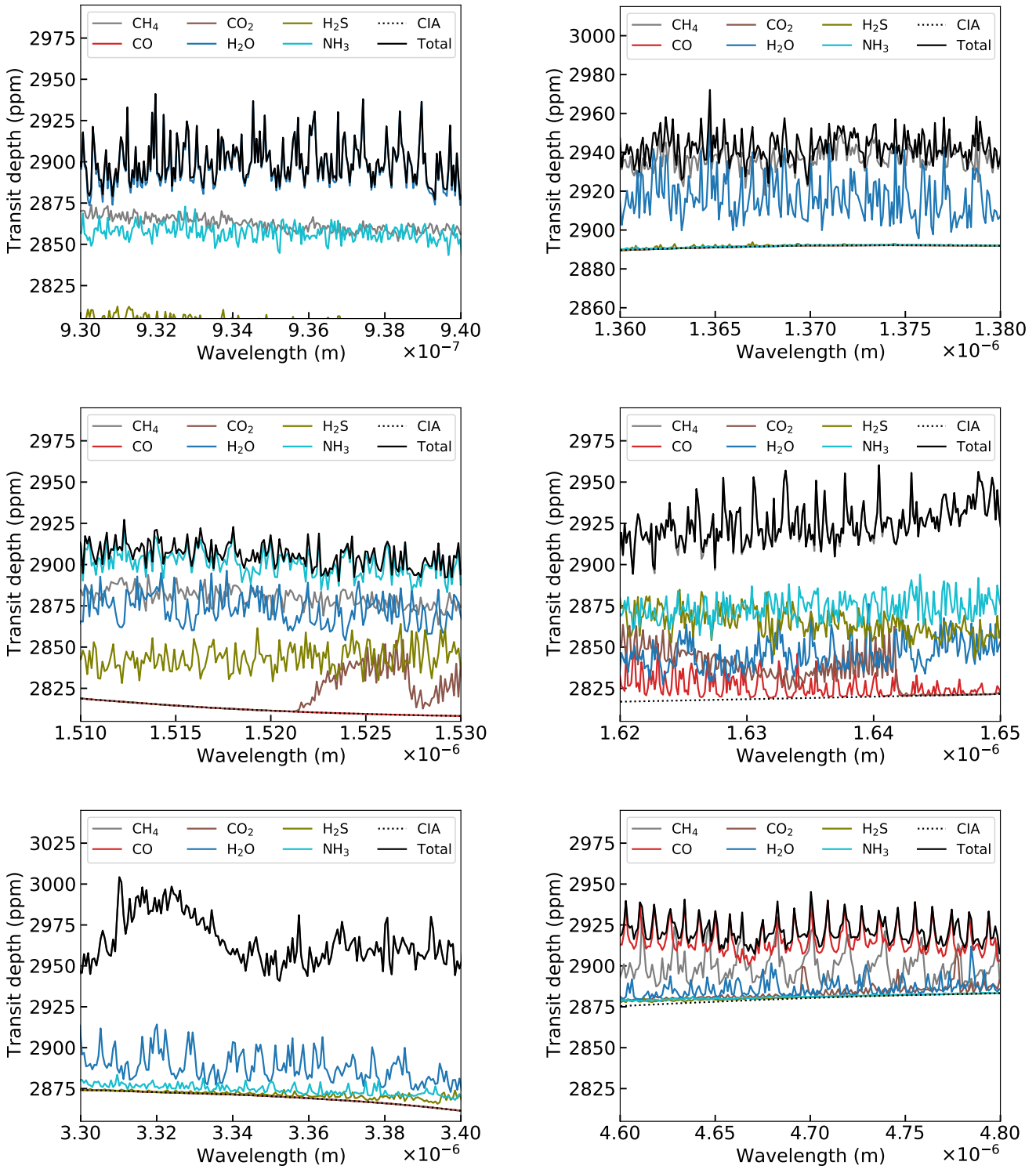


Fig. 22: Contributions within some spectral ranges of a selection of absorbing species to the transmission spectrum of our nominal model ( $175 (Z/H)_{\odot}$ ) at nominal irradiation and a resolution of  $0.5 \text{ cm}^{-1}$  (resolving power of 20 000 at  $1 \mu\text{m}$ ). The spectral contribution of individual species takes the CIA and Rayleigh scattering (dotted curve) into account.

**Acknowledgements.** D. B. acknowledges financial support from the ANR project "e-PYTHEAS" (ANR-16-CE31-0005-01). We acknowledge support from the Programme National de Planétologie of INSU/CNRS co-funded by CNES. We thank M. Rey for providing the TheoReTS  $\text{CH}_4$  line lists up to  $13400 \text{ cm}^{-1}$  over the whole Exo-REM temperature grid. We thank O. Venot for providing us with the results from Venot et al. (2020)'s thermochemical model for K2-18b. We thank J. Leconte for his valuable insight on tidal heating.

## References

- Al-Refaie, A. F., Changeat, Q., Waldmann, I. P., & Tinetti, G. 2019, arXiv preprint arXiv:1912.07759  
Allard, N. F., Kielkopf, J. F., Spiegelman, F., Tinetti, G., & Beaulieu, J. P. 2012, *A&A*, 543, A159  
Allard, N. F., Spiegelman, F., & Kielkopf, J. F. 2016, *A&A*, 589, A21  
Atreya, S. K., Crida, A., Guillot, T., et al. 2018, *Saturn in the 21st Century*, 20, 5

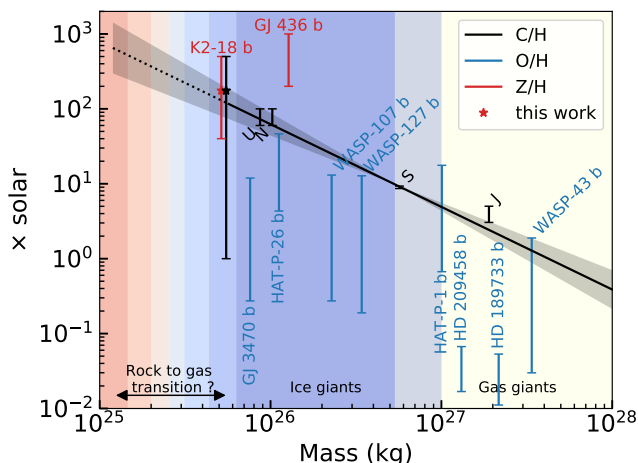


Fig. 23: Atmospheric metallicity as a function of mass for a selection of planets. The Jupiter (J), Saturn (S), Uranus (U), and Neptune (N) C/H are taken respectively from Wong et al. (2004), Fletcher et al. (2009), Sromovsky et al. (2011) and Karkoschka & Tomasko (2011) (values compiled in Atreya et al. 2018). The data for GJ436b and WASP-127b are taken respectively from Morley et al. (2017) and Skaf et al. (2020), while the data for all the other planets are taken from Welbanks et al. (2019). The black area represents the  $1\sigma$  C/H against mass trend for Jupiter, Saturn, Uranus, and Neptune resulting from a linear fit. The fit is  $\log_{10}((Z/H)/(Z/H)_{\odot}) = -1.10 \pm 0.21 \log_{10}(M[\text{kg}]) + 30.5 \pm 5.5$ . The error bars of our results correspond to the simulations that were within the  $1\sigma$  confidence interval against Tsiaras et al. (2019) data in the 'free C/H' scenario. Our C/H results were slightly shifted to the right for clarity. The O/H ratios in the other works were estimated assuming  $[\text{H}_2] + [\text{He}] + [\text{H}_2\text{O}] + [\text{CH}_4] = 1$  and a solar He/H.

Azzam, A. A. A., Tennyson, J., Yurchenko, S. N., & Naumenko, O. V. 2016, Monthly Notices of the Royal Astronomical Society, 460, 4063  
 Baudino, J. L., Bézard, B., Boccaletti, A., et al. 2015, A&A, 582, A83  
 Baudino, J. L., Mollière, P., Venot, O., et al. 2017, The Astrophysical Journal, 850, 150  
 Benneke, B., Knutson, H., Lothringer, J., et al. 2019a, Nature Astronomy, 3, 813  
 Benneke, B., Knutson, H. A., Lothringer, J., et al. 2019b, Nature Astronomy, 3, 813  
 Benneke, B. & Seager, S. 2013, The Astrophysical Journal, 778, 153  
 Benneke, B., Werner, M., Petigura, E., et al. 2017, The Astrophysical Journal, 834, 187  
 Bernath, P. F. 2020, Journal of Quantitative Spectroscopy and Radiative Transfer, 240, 106687  
 Bézard, B., Charnay, C., & Blain, D. 2020, Methane as a dominant absorber in the habitable-zone sub-Neptune K2-18 b, Nature Astronomy, submitted  
 Borysow, A. 2002, A&A, 390, 779  
 Borysow, A., Jørgensen, U. G., & Fu, Y. 2001, Journal of Quantitative Spectroscopy and Radiative Transfer, 68, 235  
 Brogi, M., de Kok, R. J., Albrecht, S., et al. 2016, The Astrophysical Journal, 817, 106  
 Brown, L. R. & Peterson, D. B. 1994, Journal of molecular spectroscopy, 168, 593  
 Burch, D. E., Gryvnak, D. A., Patty, R. R., & Bartky, C. E. 1969, J. Opt. Soc. Am., 59, 267  
 Burrows, A., Marley, M. S., & Sharp, C. M. 2000, The Astrophysical Journal, 531, 438  
 Charnay, B., Bézard, B., Baudino, J. L., et al. 2018, The Astrophysical Journal, 854, 172  
 Chase, M. 1998, NIST-JANAF Thermochemical Tables, Tech. rep.  
 Chen, J. & Kipping, D. 2016, The Astrophysical Journal, 834, 17  
 Cloutier, R., Astudillo-Defru, N., Doyon, R., et al. 2019, A&A, 621, A49  
 Coles, P. A., Yurchenko, S. N., & Tennyson, J. 2019, Monthly Notices of the Royal Astronomical Society, 490, 4638

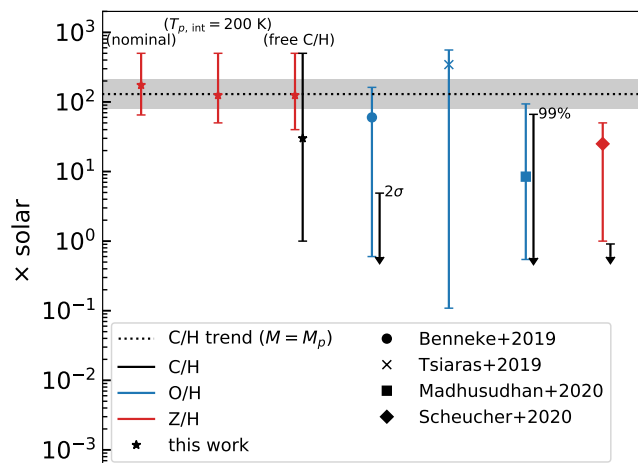


Fig. 24: Summary of our results and results of other teams on K2-18b metallicity. The error bars of our results corresponds to the simulations that were within the  $1\sigma$  confidence level against Tsiaras et al. (2019) data. The O/H and C/H ratio of the other works were estimated assuming  $[\text{H}_2] + [\text{He}] + [\text{H}_2\text{O}] + [\text{CH}_4] = 1$  and a solar He/H. The C/H upper limit of Benneke et al. (2019a) and Madhusudhan et al. (2020) corresponds respectively to the  $2\sigma$  and the 99% upper limit. The dotted line represents the metallicity expected for the mass of K2-18 b using the linear fit in Figure 23, based on solar-system C/H ratios.

Feroz, F., Hobson, M. P., & Bridges, M. 2009, Monthly Notices of the Royal Astronomical Society, 398, 1601  
 Fletcher, L. N., Orton, G. S., Teanby, N. A., Irwin, P. G. J., & Bjoeraker, G. L. 2009, Icarus, 199, 351  
 Fortney, J. J., Mordasini, C., Nettelmann, N., et al. 2013, The Astrophysical Journal, 775, 80  
 Fouchet, T., Orton, G., Irwin, P. G. J., Calcutt, S. B., & Nixon, C. A. 2004, Icarus, 170, 237  
 Fray, N. & Schmitt, B. 2009, Planetary and Space Science, 57, 2053  
 Fulton, B. J., Petigura, E. A., Howard, A. W., et al. 2017, The Astronomical Journal, 154, 109  
 Furi, E. & Marty, B. 2015, Nature Geoscience, 8, 515  
 Gomes, G. & Ferraz-Mello, S. 2020, Monthly Notices of the Royal Astronomical Society, 494, 5082  
 Guinan, E. F. & Engle, S. G. 2019, Research Notes of the AAS, 3, 189  
 Harris, G. J., Tennyson, J., Kaminsky, B. M., Pavlenko, Y. V., & Jones, H. R. A. 2006, Monthly Notices of the Royal Astronomical Society, 367, 400  
 Hartmann, J. M., Boulet, C., Brodbeck, C., et al. 2002, Journal of Quantitative Spectroscopy and Radiative Transfer, 72, 117  
 Howett, C. J. A., Carlson, R. W., Irwin, P. G. J., & Calcutt, S. B. 2007, J. Opt. Soc. Am. B, 24, 126  
 Iaroslavtsev, E. & Podolak, M. 2007, Icarus, 187, 600  
 Karkoschka, E. & Tomasko, M. G. 2011, Icarus, 211, 780  
 Kissel, A., Sumpf, B., Kronfeldt, H. D., Tikhomirov, B. A., & Ponomarev, Y. N. 2002, Journal of Molecular Spectroscopy, 216, 345  
 Kramida, A., Ralchenko, Y., eader, J., et al. 2019, NIST Atomic Spectra Database  
 Langlois, S., Birbeck, T. P., & Hanson, R. K. 1994, Journal of Molecular Spectroscopy, 167, 272  
 Lellouch, E., Bézard, B., Fouchet, T., et al. 2001, A&A, 370, 610  
 Lerot, C., Walrand, J., Blanquet, G., Bouanich, J. P., & Lepère, M. 2003, Journal of Molecular Spectroscopy, 219, 329  
 Lide, D. 2009, CRC Handbook of Chemistry and Physics, ed. by DR Lide, 90th  
 Lin, J.-F., Militzer, B., Struzhkin, V. V., et al. 2004, The Journal of Chemical Physics, 121, 8423  
 Lodders, K. 1999, Journal of Physical and Chemical Reference Data, 28, 1705  
 Lodders, K. 2002, The Astrophysical Journal, 577, 974  
 Lodders, K. 2010, Formation and Evolution of Exoplanets, by Rory Barnes. Wiley, 2010, ISBN: 978-3-527-40896-2, p. 157, 157  
 Lodders, K. 2019, arXiv preprint arXiv:1912.00844  
 Madhusudhan, N., Nixon, M. C., Welbanks, L., Piette, A. A. A., & Booth, R. A. 2020, The Astrophysical Journal, 891, L7  
 Mamajek, E., Prsa, A., Torres, G., et al. 2015, arXiv preprint arXiv:1510.07674

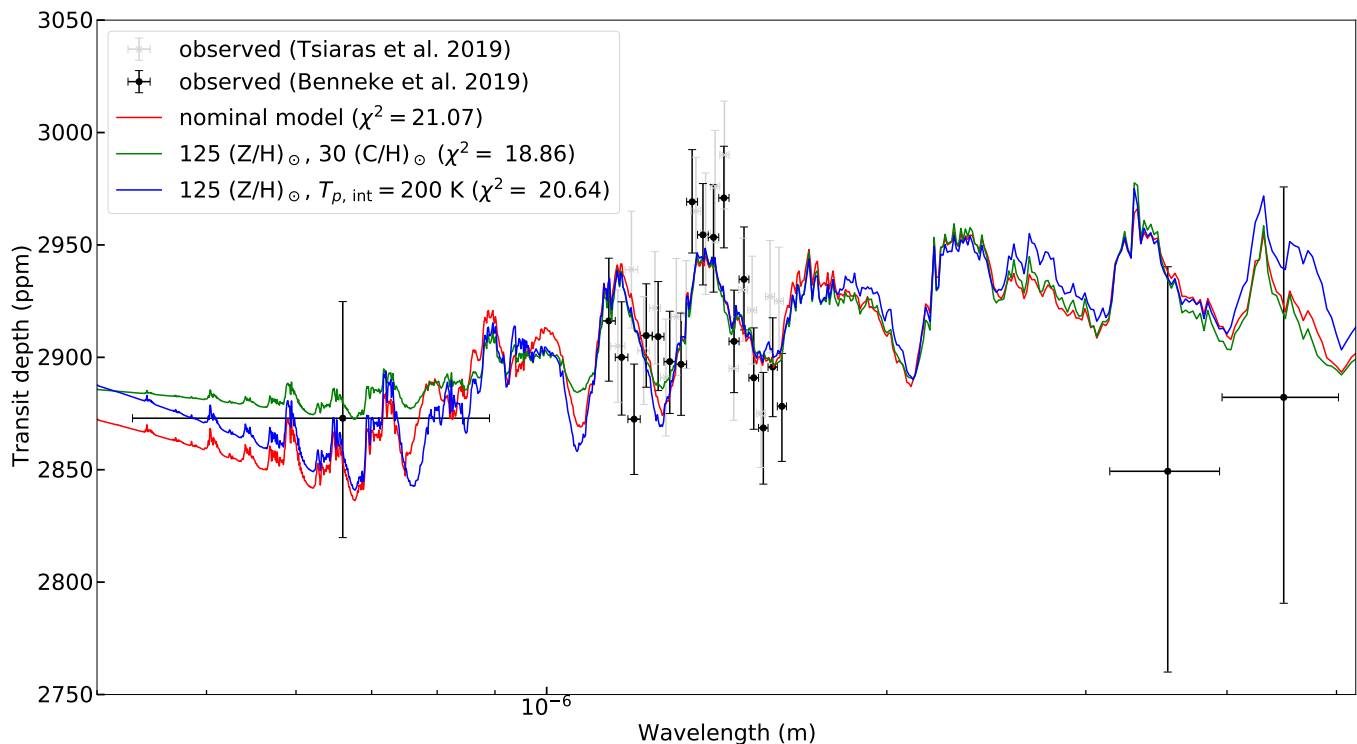


Fig. 25: Comparison of K2-18b transmission spectrum best-fits for three different scenarios. Red: 175 (Z/H) $_{\odot}$ , 175 (C/H) $_{\odot}$ ,  $K_{zz} = 10^6$  cm $^2$ ·s $^{-1}$ ,  $T_{p,int} = 80$  K. Green: 125 (Z/H) $_{\odot}$ , 30 (C/H) $_{\odot}$ ,  $K_{zz} = 10^6$  cm $^2$ ·s $^{-1}$ ,  $T_{p,int} = 80$  K. Blue: 125 (Z/H) $_{\odot}$ , 125 (C/H) $_{\odot}$ ,  $K_{zz} = 10^{10}$  cm $^2$ ·s $^{-1}$ ,  $T_{p,int} = 200$  K. The  $\chi^2$  against Benneke et al. (2019a) data is indicated in parentheses.

- Margolis, J. S. 1996, *Journal of Quantitative Spectroscopy and Radiative Transfer*, 55, 823
- McKemmish, L. K., Yurchenko, S. N., & Tennyson, J. 2016, *Monthly Notices of the Royal Astronomical Society*, 463, 771
- Mlawer, E. J., Payne, V. H., Moncet, J. L., et al. 2012, *Philosophical Transactions: Mathematical, Physical and Engineering Sciences*, 370, 2520
- Morley, C. V., Knutson, H., Line, M., et al. 2017, *The Astronomical Journal*, 153, 86
- Nemtchinov, V., Sung, K., & Varanasi, P. 2004, *Journal of Quantitative Spectroscopy and Radiative Transfer*, 83, 243
- Niemann, H. B., Atreya, S. K., Carignan, G. R., et al. 1998, *Journal of Geophysical Research: Planets*, 103, 22831
- Otegi, J. F., Bouchy, F., & Helled, R. 2020, *A&A*, 634, A43
- Pine, A. S. 1992, *The Journal of Chemical Physics*, 97, 773
- Rey, M., Nikitin, A. V., & Tyuterev, V. G. 2017, *The Astrophysical Journal*, 847, 105
- Richard, C., Gordon, I. E., Rothman, L. S., et al. 2012, *Journal of Quantitative Spectroscopy and Radiative Transfer*, 113, 1276, three Leaders in Spectroscopy
- Rinsland, C. P., [Malathy Devi], V., Smith, M. A. H., et al. 2003, *Journal of Quantitative Spectroscopy and Radiative Transfer*, 82, 343, the HITRAN Molecular Spectroscopic Database: Edition of 2000 Including Updates of 2001.
- Robie, R. & Hemingway, B. 1995, *US Geol. Survey Bull.*, vol. 2131, p. 461-461 (1995), 2131, 461
- Rogers, L. A. & Seager, S. 2010, *The Astrophysical Journal*, 712, 974
- Rothman, L. S., Gordon, I. E., Barber, R. J., et al. 2010, *Journal of Quantitative Spectroscopy and Radiative Transfer*, 111, 2139, xVIth Symposium on High Resolution Molecular Spectroscopy (HighRes-2009)
- Scheucher, M., Wunderlich, F., Grenfell, J. L., et al. 2020, *The Astrophysical Journal*, 898, 44
- Schwenke, D. W. 1998, *Faraday Discuss.*, 109, 321
- Seager, S., Kuchner, M., Hier-Majumder, C. A., & Militzer, B. 2007, *The Astrophysical Journal*, 669, 1279
- Skaf, N., Bieger, M. F., Edwards, B., et al. 2020, *The Astronomical Journal*, 160, 109
- Snellen, I., De Kok, R., De Mooij, E., & Albrecht, S. 2010, *Nature*, 465, 1049
- Sousa-Silva, C., Al-Refaie, A. F., Tennyson, J., & Yurchenko, S. N. 2014, *Monthly Notices of the Royal Astronomical Society*, 446, 2337
- Sromovsky, L. A., Fry, P. M., & Kim, J. H. 2011, *Icarus*, 215, 292
- Stull, D. 1947, *Industrial & Engineering Chemistry*, 39, 540
- Teanby, N. A., Fletcher, L. N., Irwin, P. G. J., Fouchet, T., & Orton, G. S. 2006, *Icarus*, 185, 466
- Tsiaras, A., Waldmann, I., Tinetti, G., Tennyson, J., & Yurchenko, S. 2019, *Nature Astronomy*, 3, 1086
- Tsiaras, A., Waldmann, I. P., Zingales, T., et al. 2018, *The Astronomical Journal*, 155, 156
- Valencia, D., Guillot, T., Parmentier, V., & Freedman, R. 2013, *The Astrophysical Journal*, 775, 10
- Venot, O., Cavalié, T., Bounaceur, R., et al. 2020, *A&A*, 634, A78
- Wagner, W. & Pruss, A. 1993, *Journal of Physical and Chemical Reference Data*, 22, 783
- Wagner, W., Saul, A., & Pruss, A. 1994, *Journal of Physical and Chemical Reference Data*, 23, 515
- Wakeford, H. R., Sing, D. K., Kataria, T., et al. 2017, *Science*, 356, 628
- Wang, D., Lunine, J. I., & Mousis, O. 2016, *Icarus*, 276, 21
- Welbanks, L., Madhusudhan, N., Allard, N. F., et al. 2019, *The Astrophysical Journal*, 887, L20
- Wilzewski, J. S., Gordon, I. E., Kochanov, R. V., Hill, C., & Rothman, L. S. 2016, *Journal of Quantitative Spectroscopy and Radiative Transfer*, 168, 193
- Wong, M. H., Mahaffy, P. R., Atreya, S. K., Niemann, H. B., & Owen, T. C. 2004, *Icarus*, 171, 153
- Woodfield, B. F., Shapiro, J. L., Stevens, R., et al. 1999, *The Journal of Chemical Thermodynamics*, 31, 1573
- Yurchenko, S. N. 2015, *Journal of Quantitative Spectroscopy and Radiative Transfer*, 152, 28
- Zahnle, K. J. & Marley, M. S. 2014, *The Astrophysical Journal*, 797, 41
- Zeng, L., Jacobsen, S. B., Sasselov, D. D., et al. 2019, *Proceedings of the National Academy of Sciences*, 116, 9723

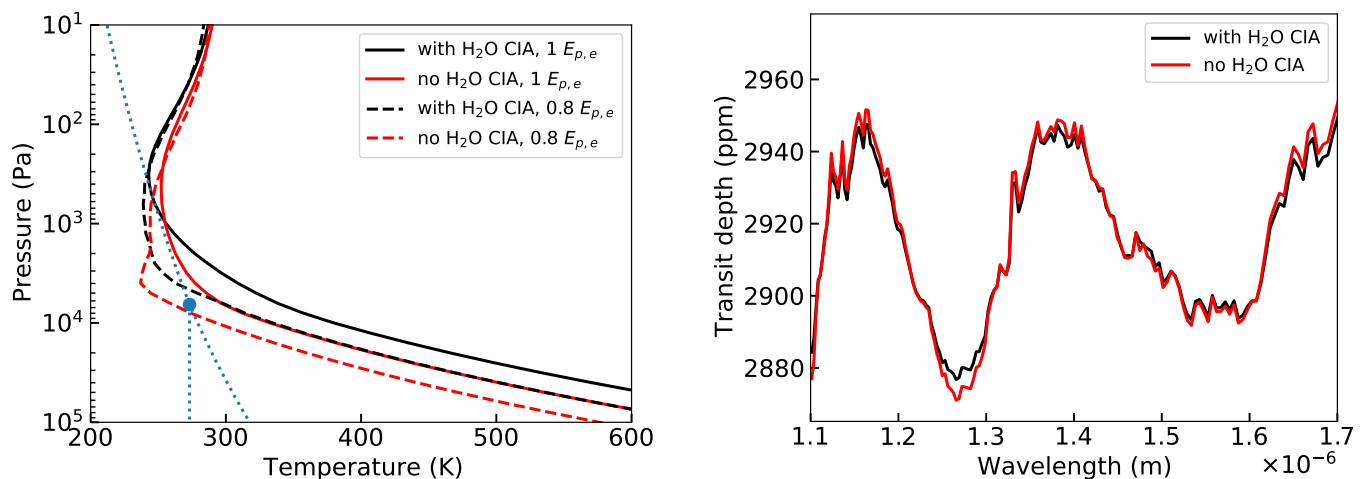


Fig. A.1: Effect of the H<sub>2</sub>O CIA at 175 (Z/H)<sub>⊙</sub> on the simulated transmission spectrum and temperature profile of K2-18b. Left: Temperature profiles. Solid black: Nominal model. Dotted-dashed black: Nominal model at 0.8 time the nominal irradiance. Red: Nominal model without H<sub>2</sub>O CIA. Dotted-dashed red: Nominal model at 0.8 times the nominal irradiance and without H<sub>2</sub>O CIA. The phase diagram of H<sub>2</sub>O is represented as dotted blue lines, the dot corresponding to the H<sub>2</sub>O triple point. Right: Transmission spectra at 0.8 time the nominal irradiance, with (black) and without (red) H<sub>2</sub>O CIA.

## Appendix A: Note on the effect of the H<sub>2</sub>O CIA

The effect of H<sub>2</sub>O CIA on transmission spectra and temperature profiles is shown in Figure A.1. In our K2-18b simulations at 175 (Z/H)<sub>⊙</sub>, we found that neglecting the H<sub>2</sub>O CIA leads to an underestimation of the atmospheric temperature by  $\approx 40$  K at 10 kPa. This can have an effect on the nature of H<sub>2</sub>O condensation as well. Taking a model with 0.8 time the nominal irradiance of K2-18b, if we include H<sub>2</sub>O CIA, we find that H<sub>2</sub>O condenses into its solid phase, whereas if we do not, it condenses into its liquid phase at slightly higher pressures ( $\approx 8$  kPa instead of 3 kPa). Moreover, because the cloud is forming lower without the CIA, it has less effect on the transmission spectrum. As a consequence, the amplitude of the absorption features of the transmission spectrum is increased. However, the effect on the temperature profile is smaller at low metallicities, with a temperature difference at 10 kPa reaching 20 K at 30 (Z/H)<sub>⊙</sub>, and 2 K at 3 (Z/H)<sub>⊙</sub>, at  $\approx 300$  kPa for both cases.

CIA are induced by molecules colliding with themselves or other species. On planets with low metallicity, H<sub>2</sub>-H<sub>2</sub> and H<sub>2</sub>-He collisions are the only significant contributors to CIA because species other than H<sub>2</sub> and He are present in low quantities. However, this no longer holds true at higher metallicity. As the abundance of other species increases, their CIA increase which has an overall warming effect on the atmosphere.

## Appendix B: TauREx 3 retrievals

From our TauREx 3 retrievals, we found an Atmospheric Detectability Index (ADI, see Tsiaras et al. 2018) of  $\geq 1.17$ , including only CH<sub>4</sub> (2.12 $\sigma$ , or 3:1 relative odds), and  $\geq 6.37$  (3.99 $\sigma$ , or 584:1 relative odds), including at least H<sub>2</sub>O, indicating 'weak' to 'strong' detections of atmospheric absorptions. Similarly to Madhusudhan et al. (2020), we find only a 'weak' detection of clouds by comparing similar models with and without clouds: the difference in log-evidence is at most 1.04 (2.05 $\sigma$  or 2.8:1 relative odds) with our CH<sub>4</sub>-only models and at least 0.29 (1.48 $\sigma$  or 1.3:1 relative odds) with our H<sub>2</sub>O-only models. Comparing our 'all absorbers with clouds' model with our 'no H<sub>2</sub>O' and 'no CH<sub>4</sub>' models, we also find that H<sub>2</sub>O is detected at 273:1 (3.79 $\sigma$ , that is, a 'strong' detection), while CH<sub>4</sub> is detected at 1.30:1 (1.44 $\sigma$ , meaning a 'not significant' detection).

Regarding our retrieval with all absorbers and clouds (see Figure 18), our retrieved VMR of H<sub>2</sub>O (0.072–5.3%) is similar to what Benneke et al. (2019a) found (0.033–8.9%). Our 2 $\sigma$  (95.4%) upper limits for CO, CO<sub>2</sub>, NH<sub>3</sub>, and N<sub>2</sub> are respectively 4.39%, 0.789%, 0.002%, and 2.73%, all lower than those from Benneke et al. (2019a) (7.45%, 2.4%, 13.5%, and 10.9%), especially for NH<sub>3</sub>. The cloud top pressure we retrieve (1.8–66.1 kPa) is slightly higher than theirs (0.77–13.9 kPa). From our Exo-REM simulations, this level corresponds more to NH<sub>4</sub>Cl condensation than to H<sub>2</sub>O condensation, but we showed that including NH<sub>4</sub>Cl clouds does not significantly enhance our fits (see Section 4.2).